Monthly Notices
of the
ROYAL ASTRONOMICAL SOCIETY

MNRAS **458,** 1311–1329 (2016) doi:10.1093/mnras/stw354
Advance Access publication 2016 February 15

Short-term X-ray spectral variability of the quasar PDS 456 observed in a low-flux state

G. A. Matzeu,[1⋆] J. N. Reeves,[1,2] E. Nardini,[1] V. Braito,[2,3] M. T. Costa,[1] F. Tombesi[4,5] and J. Gofford[1]

[1]*Astrophysics Group, School of Physical and Geographical Sciences, Keele University, Keele, Staffordshire ST5 5BG, UK*
[2]*Center for Space Science and Technology, University of Maryland Baltimore County, 1000 Hilltop Circle, Baltimore, MD 21250, USA*
[3]*INAF Osservatorio Astronomico di Brera, Via Bianchi 46, I-23807 Merate (LC), Italy*
[4]*X-ray Astrophysics Laboratory, NASA/Goddard Space Flight Center, Greenbelt, MD 20771, USA*
[5]*Department of Astronomy and CRESST, University of Maryland, College Park, MD 20742, USA*

Accepted 2016 February 11. Received 2016 February 11; in original form 2015 June 10

ABSTRACT

We present a detailed analysis of a recent, 2013 *Suzaku* campaign on the nearby ($z = 0.184$) luminous ($L_{\rm bol} \sim 10^{47}$ erg s^{-1}) quasar PDS 456. This consisted of three observations, covering a total duration of ∼1 Ms and a net exposure of 455 ks. During these observations, the X-ray flux was unusually low, suppressed by a factor of >10 in the soft X-ray band when compared to previous observations. We investigated the broad-band continuum by constructing a spectral energy distribution (SED), making use of the optical/UV photometry and hard X-ray spectra from the later simultaneous *XMM–Newton* and *NuSTAR* campaign in 2014. The high-energy part of this low-flux SED cannot be accounted for by physically self-consistent accretion disc and corona models without attenuation by absorbing gas, which partially covers a substantial fraction of the line of sight towards the X-ray continuum. At least two layers of absorbing gas are required, of column density $\log(N_{\rm H,low}/{\rm cm}^{-2}) = 22.3 \pm 0.1$ and $\log(N_{\rm H,high}/{\rm cm}^{-2}) = 23.2 \pm 0.1$, with average line-of-sight covering factors of ∼80 per cent (with typical ∼5 per cent variations) and 60 per cent (±10–15 per cent), respectively. During these observations PDS 456 displays significant short-term X-ray spectral variability, on timescales of ∼100 ks, which can be accounted for by variable covering of the absorbing gas along the line of sight. The partial covering absorber prefers an outflow velocity of $v_{\rm pc} = 0.25^{+0.01}_{-0.05}\,c$ at the >99.9 per cent confidence level over the case where $v_{\rm pc} = 0$. This is consistent with the velocity of the highly ionized outflow responsible for the blueshifted iron K absorption profile. We therefore suggest that the partial covering clouds could be the denser, or clumpy part of an inhomogeneous accretion disc wind. Finally estimates are placed upon the size-scale of the X-ray emission region from the source variability. The radial extent of the X-ray emitter is found to be of the order ∼15–20$R_{\rm g}$, although the hard X-ray (>2 keV) emission may originate from a more compact or patchy corona of hot electrons, which is typically ∼6–8$R_{\rm g}$ in size.

Key words: galaxies: active – galaxies: nuclei – quasars: individual: PDS 456 – X-rays: galaxies.

1 INTRODUCTION

Outflows are now considered an essential component in the overall understanding of active galactic nuclei (AGN). These winds are thought to occur as a result of the accretion process (King 2003; Ohsuga et al. 2009), and they can provide a link between the black hole mass and the velocity dispersion of the stars in the bulge of a galaxy, such as seen with the M–σ relation (Ferrarese & Merritt 2000; Gebhardt et al. 2000). Several works have tried to understand this relation in terms of the negative mechanical feedback provided by winds produced by an accreting supermassive black hole (e.g. King 2003, 2010; Di Matteo, Springel & Hernquist 2005; McQuillin & McLaughlin 2013). A number of massive and high-velocity outflows have been detected in luminous AGN (Chartas, Brandt & Gallagher 2003; Reeves, O'Brien & Ward 2003; Pounds et al. 2003) through the presence of resonance iron K-shell absorption lines blueshifted to energies of $E > 7$ keV (in the rest frame).

The importance of these winds is supported by their frequent detection, as they are observed in the X-ray spectra of approximately

⋆ E-mail: g.matzeu@keele.ac.uk

40 per cent of AGN (Tombesi et al. 2010; Gofford et al. 2013), suggesting that their geometry is characterized by a wide solid angle. This was recently confirmed in the quasar PDS 456 by Nardini et al. (2015, hereafter N15). These fast outflows are characterized by a considerably high column density ($N_{\rm H} \sim 10^{23}$ cm^{-2}) and a mean velocity $\langle v_{\rm w} \rangle \sim 0.1\,c$ (Tombesi et al. 2010). However, the velocity of the Fe K absorbers can cover a wide range, from as low as a few $\times$ 100–1000 km s^{-1} (more typical of what is seen in the soft X-ray warm absorbers; Kaastra et al. 2000; Blustin et al. 2005; McKernan, Yaqoob & Reynolds 2007) up to mildly relativistic values of $\sim$0.2–0.4 c in the more extreme cases (e.g. Chartas et al. 2002; Reeves et al. 2009, hereafter R09). These high velocities can result in a large amount of mechanical power, possibly exceeding the 0.5–5 per cent of the bolometric luminosity $L_{\rm bol}$ required for a significant AGN feedback contribution to the evolution of the host galaxy (King 2003; King & Pounds 2003; Di Matteo et al. 2005; Hopkins & Elvis 2010; Tombesi et al. 2015).

The primary X-ray emission of AGN is thought to originate from 'seed' UV disc photons that are Compton (up)scattered in a corona of relativistic electrons (Haardt & Maraschi 1991, 1993), producing the hard X-ray tail usually phenomenologically described by means of a simple power law. The AGN X-ray variability could be characterized by either intrinsic fluctuating spectral and temporal behaviour (e.g. Marshall, Warwick & Pounds 1981; Green, McHardy & Lehto 1993) or the presence of absorbing gas in the line of sight (Risaliti et al. 2009). The latter case may be seen as changes in the covering fraction of a partial covering absorber (e.g. Turner et al. 2011). This may favour in particular the explanation of the X-ray variability of several AGN, whose low flux and hard broad-band spectra are possibly due to partial occultation by absorbing clouds (e.g. Risaliti et al. 2005; Turner et al. 2008; Behar et al. 2010). Since the last decade, partial covering scenarios have been successful in explaining the complex X-ray spectral properties of AGN in different energy bands such as: pronounced continuum curvature below 10 keV (e.g. Miller, Turner & Reeves 2008), rapid spectral variability (e.g. Nardini & Risaliti 2011), X-ray occultation (e.g. Risaliti et al. 2007), and pronounced hard excesses above 10 keV (e.g. Turner et al. 2009; Tatum et al. 2013). In the latter case, however, reflection models have also been invoked to explain some sources with strong hard excesses (e.g. Nardini et al. 2011; Risaliti et al. 2013).

The luminous radio-quiet quasar PDS 456 is located at a redshift of $z = 0.184$ (Torres et al. 1997), and it has a de-reddened absolute magnitude of $M_B \sim -27$ and a bolometric luminosity of $L_{\rm bol} \sim 10^{47}$ erg s^{-1} (Simpson et al. 1999; Reeves et al. 2000). It is comparable in luminosity to the radio-loud quasar 3C 273, making it the most luminous quasar in the local Universe ($z < 0.3$). Such a high luminosity is more typical of quasars at redshift $z = 2$–3, considered the peak of the quasar epoch, where black hole feedback was thought to play a key role in the evolution of galaxies (Di Matteo et al. 2005). The extreme X-ray nature of PDS 456 was first noticed by Reeves et al. (2000), where very rapid X-ray variability, on time-scales of $\sim$15 ks, was observed from *RXTE* monitoring observations in the 3–10 keV band. This indicates, by the light-crossing time argument, a very compact X-ray source of a few gravitational radii ($R_{\rm g}$) in extent (where $R_{\rm g} = GM_{\rm BH}/c^2$). A short (40 ks) observation carried out with *XMM–Newton* in 2001 detected a strong absorption trough in the3 iron K band, above 7 keV, possibly attributed to the highly ionized iron K-shell feature with an associated outflow velocity of $v_{\rm w} \gtrsim 0.1\,c$ (Reeves et al. 2003). A longer (190 ks) 2007 *Suzaku* observation 'cemented' the evidence for this fast outflow, revealing two highly significant absorption lines centred at 9.08 and 9.66 keV in the quasar rest frame, where no strong atomic transitions are otherwise expected. The association of these lines to the nearest expected strong line, the Fe XXVI Lyα transition at 6.97 keV, implied an outflow velocity of $\sim$0.25–0.30 c (R09). Similarly, in a more recent (2011) 120 ks *Suzaku* follow-up observation, a broad absorption trough at $\sim$9 keV (in the source rest frame) was again found, confirming that in both the 2007 and 2011 observations the changes in the absorption features could be due to the same flow of gas in photoionization equilibrium with the emergent X-ray emission (Reeves et al. 2014, hereafter R14). Furthermore, in a recent series of five simultaneous observations with *XMM–Newton* and *NuSTAR* in 2013–2014, N15 resolved a fast ($\sim$0.25 c) P-Cygni like profile at Fe K, showing that the absorption originates from a wide angle accretion disc wind. Indeed, PDS 456 has a proven track record of strong X-ray spectral variability over the last decade, likely due to absorption and intrinsic continuum variations (Behar et al. 2010).

Here, we present a long ($\sim$1 Ms duration) 2013 *Suzaku* campaign carried out in order to determine the time-scales through which both the X-ray absorption and continuum variations occur, by directly measuring the absorber's behaviour on time-scales of tens of ks (corresponding to a light-crossing time of a few $R_{\rm g}$ for $M_{\rm BH} \sim 10^9$ M$_\odot$). An initial analysis of this data set has been presented in Gofford et al. (2014, hereafter G14), focusing on the variability of iron K absorption feature. In this paper, we investigate in more detail the broad-band continuum and absorption variability.

2 DATA REDUCTION

In this work the events and spectra adopted are essentially the same as in G14, with the only difference being a further improvement on the constraint on the iron K absorption profile. This was achieved by re-binning the spectra to the half width at half-maximum (HWHM) energy resolution of the detector (i.e. $\sim$60 eV at 6 keV).

Suzaku (Mitsuda et al. 2007) observed PDS 456 between 2013 February and March through the X-ray Imaging Spectrometer (XIS; Koyama et al. 2007) and the Hard X-ray Detector (HXD; Takahashi et al. 2007), although in these observations PDS 456 was not detected in either the PIN or GSO detectors. Due to scheduling reasons the observation is constituted by three sequences (see Table 1): the first (OBSID:707035010, hereafter 2013a), obtained between 2013 February 21 and 26, has a duration of $\sim$441 ks; the second (OBSID:707035020, hereafter 2013b) and the third (OBSID:707035030, hereafter 2013c) were obtained consecutively between 2013 March 3 and 11, and have durations of $\sim$404 and $\sim$248 ks, respectively. The total duration of the campaign was $\sim$1 Ms (after allowing for a scheduling gap between the first and the second sequence), with a total net exposure of 455 ks (Table 1). For completeness, the observation details for the earlier 2007 and 2011 *Suzaku* observations, when the X-ray flux was substantially higher, are also listed in Table 1. All the spectral analysis and model fitting, performed with XSPEC v12.8.2 (Arnaud 1996), were focused on the spectra obtained by the XIS front illuminated (FI) CCDs – XIS 0 and XIS 3 – as they are characterized by a larger effective area and yet lower background in the iron K band compared to the back illuminated XIS 1 CCD. The XIS 1 spectra, although consistent with those obtained with XIS 0 and 3, are noisier at higher energies in the Fe K band.

Furthermore, as the XIS 0 and XIS 3 spectra were consistent with each other, we combined them into a single XIS-FI spectrum for all the observations. For the XIS-FI spectra, we adopted a spectral binning corresponding to the approximate HWHM resolution of

Table 1. Summary of the three 2013 observations of PDS 456 with *Suzaku* plus the 2007 and 2011 for comparison purposes.

	2007	2011	2013a	2013b	2013c
Obs. ID	701056010	705041010	707035010	707035020	707035030
Start date, Time (UT)	2007-02-24, 17:58	2011-03-16, 15:00	2013-02-21, 21:22	2013-03-03, 19:43	2013-03-08, 12:00
End date, Time (UT)	2007-03-01, 00:51	2011-03-19, 08:33	2013-02-26, 23:51	2013-03-08, 12:00	2013-03-11, 09:00
Duration (ks)	370	240	440.9	404.2	248.4
Exposure (ks)[a]	190.6	125.6	182.3	164.8	108.3
$\mathrm{Flux}^{b}_{(0.5-2)\mathrm{keV}}$	3.46	1.36	0.59	0.30	0.43
$\mathrm{Flux}^{b}_{(2-10)\mathrm{keV}}$	3.55	2.84	2.09	1.59	1.72
$\mathrm{Flux}^{b}_{(15-50)\mathrm{keV}}$	$5.7^{+2.2}_{-2.2}$	<2.5	<2.0	<2.0	<2.0

Notes. [a]Net exposure time, after background screening and dead-time correction.
[b]Observed fluxes in the 0.5–2, 2–10 and 15–50 keV bands in units $\times\ 10^{-12}$ erg cm^{-2} s^{-1} (1σ upper limits).

Table 2. Summary of the simultaneous *XMM–Newton* and *NuSTAR* observations of PDS 456 focused on observations A and E. Quantities and units are the same defined in Table 1.

	XMM/ObsA	*XMM*/ObsE	*NuSTAR*/ObsA	*NuSTAR*/ObsE
Obs. ID	0721010201	0721010601	60002032002	60002032010
Start date, Time (UT)	2013-08-27, 04:41	2014-02-26, 08:03	2013-08-27, 03:41	2014-02-26, 08:16
End date, Time (UT)	2013-08-28, 11:13	2014-02-27, 22:51	2013-08-28, 11:41	2014-02-28, 22:56
Duration (ks)	110.0	139.7	113.9	224.3
Exposure (ks)	95.7	100.3	43.8	109.7
$\mathrm{Flux}_{(0.5-2)\mathrm{keV}}$	3.8	1.6	–	–
$\mathrm{Flux}_{(2-10)\mathrm{keV}}$	6.6	2.6	6.8	2.7
$\mathrm{Flux}_{(15-50)\mathrm{keV}}$	–	–	3.9	1.2

the detector (which is ∼60 eV at 6 keV), using the `rbnpha` and `rbnrmf` FTOOLS to hardwire this binning into the spectral and response files. An additional grouping corresponding to >25 counts per spectral bin was subsequently applied to the re-binned spectra, in order to use the χ^2 minimization technique. The XIS-FI spectra are fitted over the 0.6–10 keV band, ignoring the 1.7–2.1 keV interval due to uncertainties with the XIS detector Si edge. Although not detected at hard X-rays in these observations, we obtained an upper limit to the HXD/PIN flux in 2013a between 15–50 keV, i.e. $<2.0 \times 10^{-12}$ erg cm^{-2} s^{-1}. The flux was obtained by converting the HXD/PIN count rate through WebPIMMS,[1] assuming a simple power law with $\Gamma = 2.4$ (see below). In all the subsequent spectral fits, the predicted limits to the hard X-ray flux are consistent with the above value.

Values of $H_0 = 70\,\mathrm{km\,s^{-1}\ Mpc^{-1}}$ and $\Omega_{\Lambda_0} = 0.73$ are assumed throughout and errors are quoted at the 90 per cent confidence level ($\Delta\chi^2 = 2.71$) for one parameter of interest.

3 BROADBAND SPECTRAL ANALYSIS

The 2013 *Suzaku* observations caught PDS 456 in an unusually low flux, compared to either the later simultaneous *XMM–Newton* and *NuSTAR* campaign, carried out in 2013 August/2014 February, and to the 2007 and 2011 *Suzaku* observations (Tables 1 and 2). This is shown in Fig. 1, which compares the fluxed spectra (unfolded through the instrumental response against a simple $\Gamma = 2$ power law, and not corrected for Galactic absorption) from the 2013 *Suzaku* sequences to the lowest (Obs E) and the highest (Obs A) of the five *XMM–Newton*/*NuSTAR* sequences (N15). It is clear that the 2013 *Suzaku* observations caught PDS 456 in an extended period of low flux, especially compared to the 2007 *Suzaku* or the 2013 *XMM–Newton* (Obs A) observations, when the soft X-ray band flux is typically a factor of 10 brighter. This therefore provided a unique opportunity to understand the properties of the intrinsic continuum and the reprocessing material in the low-flux state of PDS 456.

[1] https://heasarc.gsfc.nasa.gov/cgi-bin/Tools/w3pimms/w3pimms.pl

3.1 Comparison between *Suzaku* and *XMM–Newton/NuSTAR*

As a preliminary test, we parametrized the spectral differences between all the five *Suzaku* spectra in the 2–8 keV band (in order to avoid the contribution of the Fe-K absorption lines to the continuum) with a simple power-law model, where the photon indices and normalizations are allowed to vary between all the spectra. The 2011, 2013a, 2013b and 2013c are characterized by a harder spectral shape, $\Gamma = 1.94 \pm 0.04$, 1.47 ± 0.04, 1.29 ± 0.05 and 1.64 ± 0.05, respectively, compared to the 2007 spectrum ($\Gamma = 2.25 \pm 0.03$). This simple single power-law model provided a statistically very poor fit to the data, with $\chi^2/\nu = 2125/1318$. Furthermore, it is thought that the underlying continuum in PDS 456 is intrinsically steep ($\Gamma \gtrsim 2$), as evident from the 2007 observation, when the continuum was observed through little or no obscuration (R09), as well as from the *NuSTAR* observations, with typically $\Gamma \sim 2.4$ measured above 10 keV (e.g. N15). It follows that such a drastic hardening of the 2013 *Suzaku* spectra may be unphysical if simply attributed to the shape of the intrinsic continuum. On the other hand, what is seen is a series of spectra that may be affected by either complex absorption or reprocessed (reflected/scattered) emission, or the contribution of both. In addition to the harder shape of the three 2013 sequences, a deeper absorption trough is observed at ∼9 keV (in the quasar rest frame) which apparently strengthens as the observation progresses from 2013a to 2013c. In Table 3. we list the iron K emission and absorption line properties as parametrized by Gaussian profiles, whose variability will be discussed later in Section 4.1.

Generally speaking, it has been suggested that all AGN characterized by a low-flux spectrum may be reflection dominated (e.g.

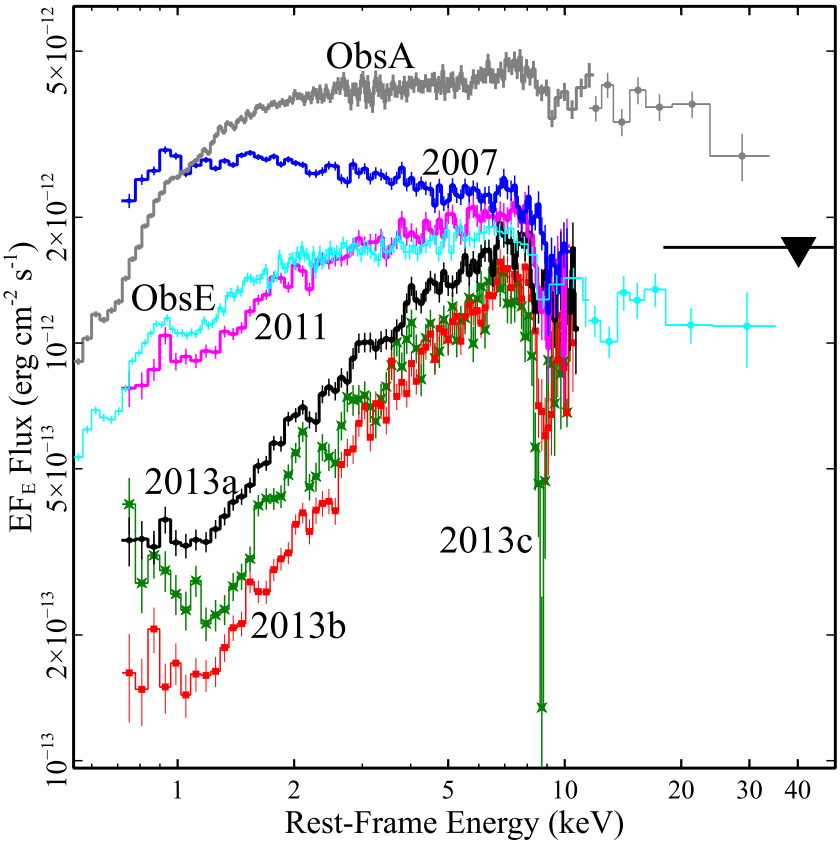

Figure 1. Spectra of the 2013 *Suzaku* observation: sequence 1 – 2013a (black, including the 15–50 keV HXD/PIN upper limit), sequence 2 – 2013b (red) and sequence 3 – 2013c (green). For comparison also the 2013 (Obs A, grey) and 2014 (Obs E, cyan) spectra of the *XMM–Newton*/*NuSTAR* campaign and the 2007 (blue) and 2011 (magenta) *Suzaku* spectra are shown. The long-term spectral variations in the soft band and in the Fe-K region, which characterize this type 1 quasar, are evident. The *Suzaku* observation in 2013 caught PDS 456 in a remarkably low-flux state compared to both earlier and subsequent observations.

Fabian et al. 2012; Gallo et al. 2013). None the less, there are some clear differences in the PDS 456 spectra, such as the non-detection of a 'Compton hump' above 10 keV (see Fig. 1 and N15), and the lack of a narrow 6.4 keV iron Kα line (see Fig. 2), which even in the 2013 low-flux state has a low upper limit on the equivalent width (EW) of <28 eV (2013a), <31 eV (2013b) and <37 eV (2013c). This rules out the presence of a distant Compton-thick reprocessor. Neither is a prominent red wing to any broad iron K emission evident, unlike what claimed in the spectra of other AGN (Fabian et al. 2002). This suggests that PDS 456 is probably not dominated by strong Compton reflection components, from either the disc or distant matter. This alternative physical interpretation and the comparison between reflection and absorption based models will be investigated in detail in a parallel paper (Costa et al. in preparation).

3.2 Modelling the broad-band SED

The spectral variability that characterizes PDS 456 is conspicuous, in particular over a six month/one year time-scale, as shown in Fig. 1. In order to gain a better understanding of this pronounced spectral variability, we first need to characterize the broad-band intrinsic continuum of PDS 456. We therefore tested whether the broad-band spectral energy distribution (SED) of PDS 456 could be described by a multitemperature Comptonized accretion disc model, using the `optxagnf` model (Done et al. 2012) in XSPEC. This model is characterized by three separate components, which are self-consistently powered by dissipation in the accretion flow: (i) the thermal emission from the outer accretion disc in the optical/UV; (ii) the up-scattering of the UV disc photons into a soft X-ray excess from a warm disc atmosphere; (iii) a high temperature Comptonization from the corona (i.e. the standard hard X-ray power-law continuum). The parameter $r_{\rm cor}$ is the coronal size that acts as a transitional radius from the colour temperature corrected blackbody emission (produced from the outer disc) to a hard power law produced through Compton up-scattering. The parameter $F_{\rm pl}$ gives the fraction of the energy released in the power-law component. The parameters kT and τ are the electron temperature and the optical depth of the soft Comptonization component, possibly originating from the warm disc atmosphere and seen as the soft excess, while $\log(L/L_{\rm Edd})$ is the Eddington ratio of the AGN (see Done et al. 2012 for more details).[2]

The form of the optical/UV to hard X-ray SED has been defined when the X-ray observations are in the 2013 *Suzaku* low flux state. To this end, we also make use of the optical/UV photometry provided by the *XMM–Newton* Optical Monitor, noting that, although the optical/UV fluxes are not simultaneous with the *Suzaku* observation six months earlier, there appears to be little variability in this band from both the *XMM–Newton* observations (to within 5 per cent) and the archival *Swift* observations over a period of ∼6 months (A. Lobban, private communication). In order to define the

[2] In this work, for simplicity, the spin parameter $a^\star$ was kept fixed to zero in all the `optxagnf` fits.

Table 3. `optxagnf` model baseline continuum parameters. ^{t} denotes that the parameter is tied during fitting. A cross-normalization factor of 0.98 ± 0.08 has been found between the non-simultaneous *Suzaku* 2013a and *NuSTAR* Obs E spectra.

Component	Parameter	2013a	2013b	2013c
Tbabs	$N_{\rm H,Gal}/{\rm cm}^{-2}$	2×10^{21}	2×10^{21}	2×10^{21}
optxagnf	$\log(L/L_{\rm Edd})$	-0.08 ± 0.10	-0.08^t	-0.08^t
	$r_{\rm cor}$ ($R_{\rm g}$)	41^{+58}_{-19}	41^t	41^t
	$kT_{\rm e}$ (eV)	468^{+156}_{-156}	468^t	468^t
	τ	$9.9^{+2.3}_{-2.4}$	$8.9^{+2.5}_{-2.7}$	9.6 ± 2.7
	Γ	2.4 ± 0.1	2.4^t	2.4^t
	$F_{\rm pl}$	$0.09^{+0.07}_{-0.04}$	$0.08^{+0.06}_{-0.03}$	$0.11^{+0.08}_{-0.04}$
$\rm pc_{low}$	$\log(N_{\rm H,low}/{\rm cm}^{-2})$	22.4 ± 0.1	22.4^t	22.4^t
	$f_{\rm cov,low}$ (per cent)	88^{+2}_{-3}	88^t	88^t
$\rm pc_{high}$	$\log(N_{\rm H,high}/{\rm cm}^{-2})$	23.1 ± 0.1	23.1^t	23.1^t
	$f_{\rm cov,high}$ (per cent)	71^{+10}_{-9}	71^t	71^t
$\rm zgauss_{em}$	Energy (keV)	6.9 ± 0.1	6.9^t	6.9^t
	EW (eV)	94^{+32}_{-26}	118^{+33}_{-36}	125^{+43}_{-31}
	σ(eV)	212^t	212^t	212^t
	Norm^a	4.6 ± 1.2	4.6^t	4.6^t
$\rm zgauss_{abs}$	Energy (keV)	$8.55^{+0.34}_{-0.26}$	8.88 ± 0.10	8.70 ± 0.07
	EW (eV)	126 ± 63	353 ± 82	530 ± 72
	σ(eV)	264^t	264^t	264^{+74}_{-56}
	norm^a	$-3.0^{+1.5}_{-0.76}$	-6.4 ± 1.4	-9.6 ± 1.3
	$(\Delta\chi^2/\Delta\nu)^b$	15/2	61/2	141/2
		$\chi^2/\nu = 522/498$		

Notes. $L/L_{\rm Edd}$: Eddington ratio
$r_{\rm cor}$ radius of the X-ray corona in $R_{\rm g}$,
$F_{\rm pl}$: fraction of the dissipated accretion energy emitted in the hard power law,
$\rm pc_{low}$, $\rm pc_{high}$: low and high column partial covering components with respective column density and covering fraction.
^{a}Gaussian emission and absorption profile normalization, in unit of 10^{-6} photons cm^{-2} s^{-1}.
^{b}Change in $\Delta\chi^2/\Delta\nu$ when the Gaussian component modelling the iron K absorption profile is removed.

hard X-ray spectral shape above 10 keV, we consider only the lowest flux (Obs E) *NuSTAR* spectrum, as it appears closest in flux to the *Suzaku* 2013a observations at 10 keV and is also consistent with the upper limit obtained for the HXD/PIN (see Tables 1, 2 and Fig. 1). The data sets were fitted simultaneously but allowing for a cross-normalization factor between the *Suzaku* 2013 and *NuSTAR* (Obs E) to account for any absolute differences in hard X-ray flux, which is found to be very close to 1.0 (i.e. 0.98 ± 0.08).

When fitting the SED with `optxagnf`, we found that some absorption is required to account for the spectral curvature above 1 keV, as shown in Fig. 3 (top panel). By adding one layer of neutral partial covering (`zpcfabs`) of column density $\log(N_{\rm H}/{\rm cm}^{-2}) = 22.47^{+0.02}_{-0.04}$ and covering fraction $f_{\rm cov} = 0.97 \pm 0.01$ (tied between the three sequences), the fit improved significantly by $\Delta\chi^2/\Delta\nu = 983/2$. However, some curvature is still present in the residuals above ∼3 keV, and the steepness of the spectral slope above 10 keV, observed with the *NuSTAR* data, is not reproduced (Fig. 3, middle panel). By adding a second layer of neutral partial covering, the fit improved by a further $\Delta\chi^2/\Delta\nu = 83/2$, yielding $\chi^2/\nu = 522/498$. In this latter case, a lower column zone ($\rm zpcfabs_{low}$) of column density $\log(N_{\rm H,low}/{\rm cm}^{-2}) = 22.4 \pm 0.1$ and covering fraction $f_{\rm cov,low} = 0.88^{+0.02}_{-0.03}$ is required to account for the absorption present in the soft X-ray band. A higher column zone ($\rm zpcfabs_{high}$), with column density of $\log(N_{\rm H,high}/{\rm cm}^{-2}) = 23.1 \pm 0.1$ and covering fraction $f_{\rm cov,high} = 0.71^{+0.10}_{-0.09}$, parametrizes the spectral curvature above 2 keV; thus it is the combination of the two zones that reproduces the complex overall spectral curvature below 10 keV.

We initially kept the partial covering column density and covering fractions tied between the three *Suzaku* sequences; in order to allow for small changes we let the `optxagnf` parameters τ and $F_{\rm pl}$ free to vary. The coronal size was also tied between the sequences, and it is found to be $r_{\rm cor} = 41^{+58}_{-19}\ R_{\rm g}$. Due to the degeneracy between the optical depth and the temperature of the warm electrons responsible for the soft excess, we kept the latter tied between the observations, yielding $kT = 468^{+156}_{-107}$ eV. The Eddington ratio $\log(L/L_{\rm Edd}) = -0.08$ implies that PDS 456 radiates close to its Eddington luminosity (∼80 per cent of $L_{\rm Edd}$); this is consistent with the expectations for PDS 456, given its black hole mass ($M_{\rm BH} \sim 10^9\ {\rm M}_\odot$) and bolometric luminosity ($L_{\rm bol} \sim 10^{47}$ erg s^{-1}). When allowing the covering fractions to vary between the three sequences, they are typically found to be within ∼10 per cent of each other, and the statistical improvement is not too drastic ($\Delta\chi^2/\Delta\nu = 13/2$), at least considering these time-averaged spectra. We note that the value of $r_{\rm cor}$ above is somewhat larger than usually expected (e.g. Risaliti et al. 2009; Reis & Miller 2013), but given our assumptions (for instance, zero black hole spin) this is regarded as a rough estimate only. If we fix $r_{\rm cor} = 10\ R_{\rm g}$ (see Section 6), we recover a fit equivalent to the case with $a^\star = 0$ above for $a^\star \sim 0.5$. In Section 5, we return to consider the spectral variability in the time-sliced spectra, where more pronounced variability is present on shorter time-scales.

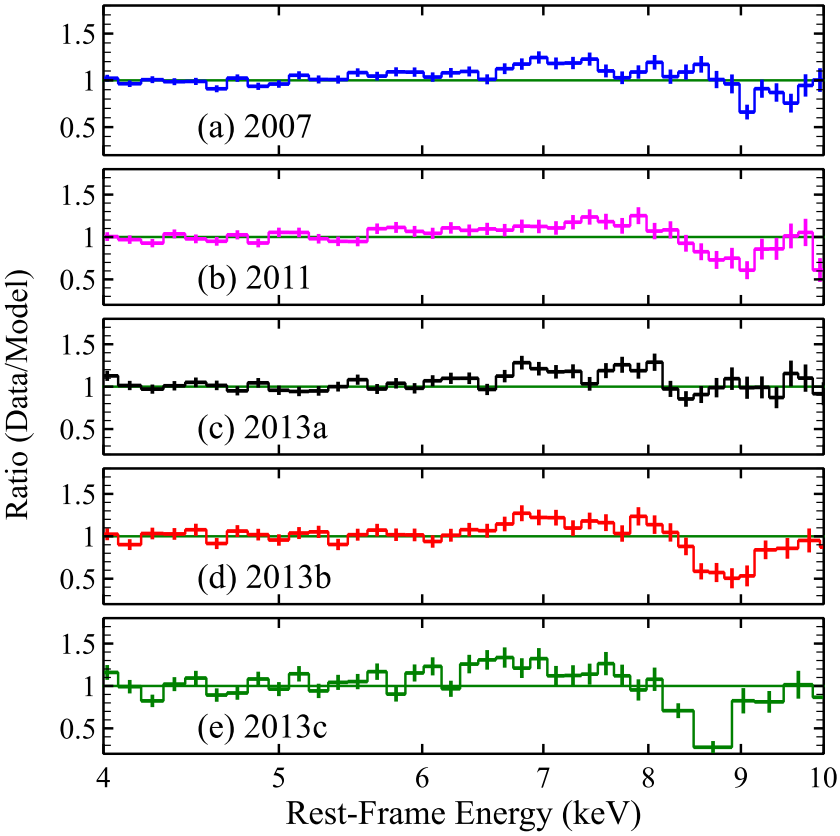

Figure 2. Fe K band of the 2007 (blue), 2011 (magenta), 2013a (black), 2013b (red) and 2013c (green) *Suzaku* observations plotted as a ratio to a phenomenological continuum fitted by excluding the observed 5–8.5 keV range. It is noticeable how in the 2013 segments, the strength of the absorption feature increases at energies $E \sim 8.5$–9 keV as the observation progresses. The broad iron K emission is rather faint and appears to be centred at ∼7 keV, while the narrow Fe Kα line at 6.4 keV is virtually absent from all the five observations.

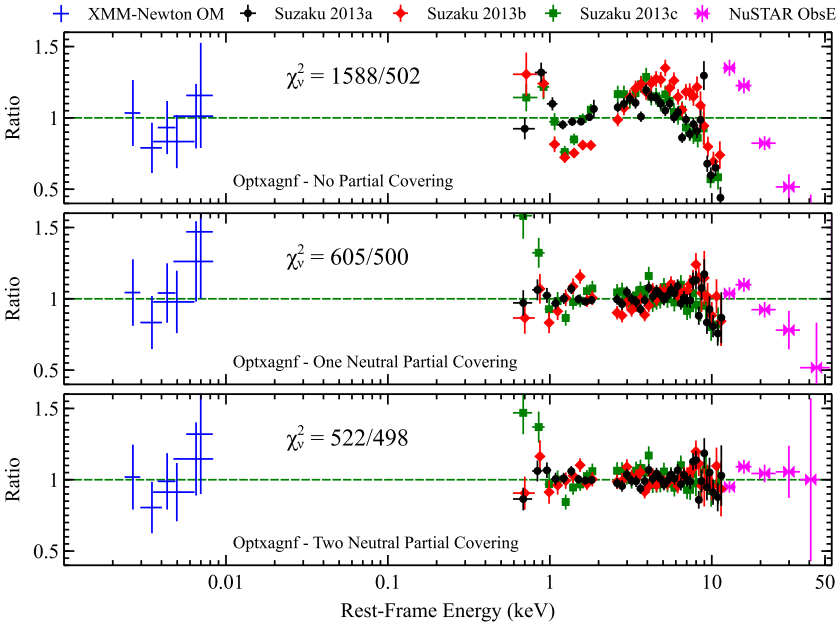

Figure 3. Residuals for the different `optxagnf` model fits over the 1 eV–50 keV energy range, plotted as data/model ratios. The spectra correspond to the *XMM–Newton* OM and *NuSTAR* from Obs E in 2014 (blue and magenta, respectively), while also plotted are the *Suzaku* 2013a (black), 2013b (red), 2013c (green) sequences. Top panel: SED fits with `optxagnf` and no partial covering absorption. Middle panel: Same as above but with the addition of one partial covering layer. Bottom panel: same as above but with two partial covering layers. For extra clarity, the spectra have been re-binned.

4 THE FE K BAND MODELLING

Having parametrized the continuum form in the previous section, here we focus on the analysis of the properties of the iron K emission and absorption profiles and on their variability over the 2013 *Suzaku* observations.

4.1 The iron K band: emission and absorption profiles

When the absorption feature, in the `optxagnf` baseline model, was fitted with a Gaussian profile ($\texttt{zgauss}_{\rm abs}$), the centroid energy at ∼8.6–8.8 keV indicates a large degree of blueshift when compared to the expected lab-frame energies of the 1s-2p lines of He- or H-like Fe at 6.7 and 6.97 keV. The absorption line EW increases by a factor of ∼5 throughout the observation, from EW $= -126 \pm 63$ eV in the 2013a sequence (improving the fit by $\Delta\chi^2/\Delta\nu = 15/2$) to EW $= -353 \pm 82$ eV in 2013b ($\Delta\chi^2/\Delta\nu = 61/2$), and EW $= -530 \pm 72$ eV in 2013c (improving considerably the fit by $\Delta\chi^2/\Delta\nu = 141/2$; see Table 3).

A cosmologically redshifted ($z = 0.184$) Gaussian component ($\texttt{zgauss}_{\rm em}$) parametrizes the ionized emission profile at 6.9 ± 0.1 keV (in the quasar rest frame), likely corresponding to the Fe XXVI Lyα resonance line, although we found that the emission profile is generally difficult to constrain in these 2013 data sets. So the nature of the iron K emission might be associated with the P-Cygni-like feature (e.g. see the Fe K profile in 2013b,c from Fig. 2) arising from the disc wind and resolved in the simultaneous *XMM–Newton* and *NuSTAR* observations carried out in late 2013/early 2014 (N15). Similar to the fit adopted in N15, the widths of the emission and the absorption Fe K profiles were tied together with a common velocity broadening of $\sigma = 264^{+74}_{-56}$ eV at the energy of the absorption line, or $\sigma = 212$ eV at 7 keV (this corresponds to a maximum velocity dispersion of $\sigma_{\rm v} \sim 9100\,{\rm km\,s^{-1}}$ or FWHM ∼21 400 km s^{-1}). This model provided a statistically very good fit ($\chi^2_\nu = 522/498$). Unsurprisingly, if the Fe K absorption feature is not accounted for the model will produce a very poor fit, i.e. $\chi^2_\nu = 717/502$.

4.1.1 *X-ray background*

Fig. 4 shows the comparison (focused on the Fe K band) between the net source spectra and the averaged background spectrum, where the shaded area indicates its maximal fluctuation during the observation. A strong background emission line, corresponding to Ni Kα, arises at ∼7.5 keV, which coincides with the observed frame energy of the Fe K absorption profile during the 2013 *Suzaku* observations. Thus it is possible that, if the background is incorrectly subtracted, it could contribute towards the absorption line feature in the source spectrum. The absorption feature is anyway variable by a factor of ∼4–5, whilst the background is almost constant (±10 per cent) across all of the 2013 observations. To be conservative, we fitted the background spectrum of 2013c (where the Fe K absorption feature is strongest) between 5–9 keV with a simple power law and a Gaussian emission profile, centred at 7.49 ± 0.03 keV. We find that by comparing the normalizations of both the Ni Kα emission ($1.2 \pm 0.3 \times 10^{-6}$ photons cm^{-2} s^{-1}) and the Fe K absorption ($-9.6 \pm 1.3 \times 10^{-6}$ photons cm^{-2} s^{-1}) lines, the former could only contribute to 12 ± 3 per cent of the latter. Consequently, there is no possibility that the background feature can account for both the observed strength and variability of the absorption line, as we would expect similar variability amplitudes from the absorption line and the Ni background line, a trend that we clearly do not observe.

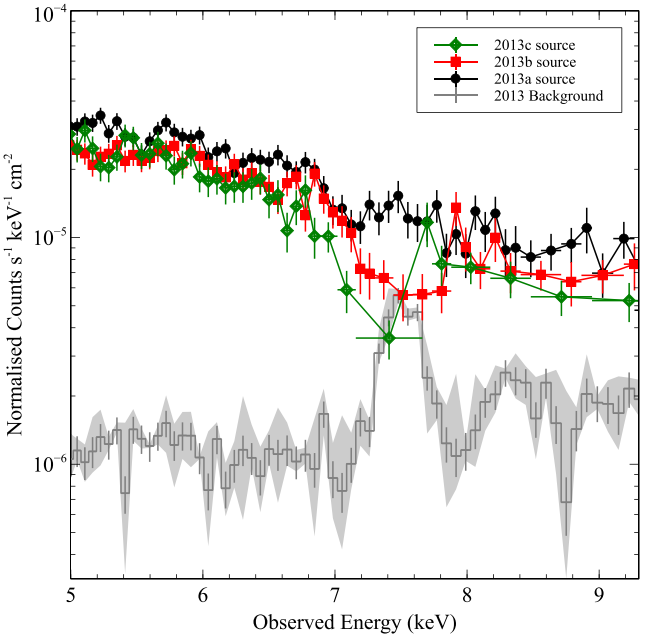

Figure 4. 2013 *Suzaku* XIS03 background subtracted source spectra versus the averaged background spectrum. The shaded area indicates the degree of the background fluctuation across the observation. A prominent background line, corresponding to Ni Kα, arises at ∼7.5 keV; this was also detected by R09 in the 2007 PDS 456 spectrum (see their Fig. 3). Unfortunately, in the 2013 spectra the centroid energy of the Ni Kα corresponds to that of the Fe K absorption feature, as the latter is shifted to lower energies compared to the 2007 observation. It is important to note the amplitude of the background variability of ±10 per cent is too small to influence the strong increase in strength of the Fe K absorption profile from the 2013a through to the 2013c observation. The source spectra are grouped to a 4σ significance for each energy bin.

Moreover, in the 2007 *Suzaku* observation (R09) the Fe K absorption lines were observed at higher energies (at 7.67 keV and 8.15 keV, respectively) and thus were clearly separated from the Ni Kα feature at 7.45 keV (see fig. 3 in R09). The level of the background relative to the source was much lower in those observations, as the source was much brighter. During the *XMM–Newton* observations of PDS 456 (N15), the overall level of the background is substantially lower (<1 per cent compared to the source spectrum), due to the smaller extraction region used. Thus for either *Suzaku* or *XMM–Newton*, the background subtraction likely makes a negligible contribution towards the absorption line.

4.2 Input SED for XSTAR

Having parametrized the iron K absorption with a simple Gaussian models, we proceed to model the iron K absorption in PDS 456 with multiplicative grids of photoionized spectra. In order to do this, we first need to characterize the input photoionizing continuum. Self-consistent XSTAR (v2.21bn13; Bautista & Kallman 2001) grids were generated using the UV to hard X-ray SED of PDS 456. Previously, G14 adopted an XSTAR absorption grid with velocity broadening $\sigma_{\rm turb} = 5000\,{\rm km\,s^{-1}}$, using a single power law of $\Gamma = 2.4$ for the 1–1000 Ryd continuum. Here, following N15, we estimated the SED of PDS 456 by using the simultaneous *XMM–Newton* and *NuSTAR* data (including six photometric bands of the Optical Monitor, see Section 3.2). We found that the SED can be approximated with a phenomenological double broken power law (see Fig. 5). This

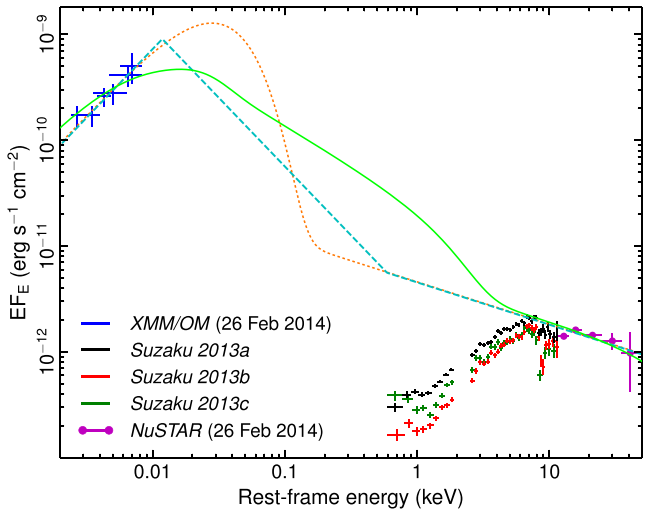

Figure 5. Optical to hard X-ray SED of PDS 456 obtained by combining the OM and *NuSTAR* (blue and magenta, respectively) from the last *XMM–Newton/NuSTAR* observation in 2014 and the 2013a,b and c sequences from the *Suzaku* campaign (black, red and green, respectively). The SED was first fitted with the `optxagnf` model (green line), and then approximated with a double broken power law (dashed cyan line) with break energies of 10 eV and 500 eV as an input for XSTAR. For comparison only, the dotted orange curve shows a disc blackbody component with temperature of 10 eV. Note that the models are corrected for absorption (either Galactic or local to the source), whereas the spectra are not.

yielded $\Gamma \sim 0.7$ in the optical/UV up to an assumed break energy of 10 eV, $\Gamma \sim 3.3$ between the optical/UV and the soft X-ray band up to the second break energy fixed at 0.5 keV, and $\Gamma = 2.4$ beyond that in the X-ray band (see Fig. 5). By adopting this model, we estimated a total 1–1000 Ryd ionizing luminosity of $L_{\rm ion} \sim 5 \times 10^{46}$ erg s^{-1}, which is also broadly consistent with the estimate derived earlier for the `optxagnf` model (Fig. 5).

Subsequently, we adopted this SED as the input continuum for our custom XSTAR grids. We investigated the effects of different velocity broadening by generating various XSTAR grids for a range of $\sigma_{\rm turb}$ values in order to provide an accurate description of the width of the Fe K absorption profile. We found that grids with lower $\sigma_{\rm turb}$ (e.g. $\sigma_{\rm turb} = 1000$–3000 km s^{-1}) result in a smaller EW of the absorption lines compared to the data, as the absorption profile saturated too quickly at a lower column density. An adequate fit to the Fe K absorption profile was achieved when we adopted a grid with $\sigma_{\rm turb} = 10\,000$ km s^{-1}; this is consistent with the velocity width measured earlier from a simple Gaussian profile. Thus we used the $\sigma_{\rm turb} = 10\,000$ km s^{-1} grid, with the input SED described above, in all the subsequent fits.

4.3 Photoionization modelling of the Fe K absorption

Having generated a suitable XSTAR grid, we used it to parametrize the Fe K absorption line. We first applied XSTAR to the 2013c spectrum, where the iron K absorption profile is stronger, in order to investigate any physical degeneracy that may arise in the model by allowing the column density and the ionization parameter[3] to vary along with the absorber's velocity. In Fig. 6 (left-hand panel), the elongated shape of the contours does indeed imply that there is some degeneracy between $N_{\rm H}$ and log (ξ). This behaviour can be attributed to the fact that most of the iron is in the He- and H-like state. Thus a gradual increase of log (ξ) would not significantly affect the line centroid energies, but it would instead increase the proportion of fully ionized iron, requiring an apparent increase in $N_{\rm H}$ to compensate for it. On the other hand, the other two contour plots (centre and right-hand panel) show no apparent degeneracies between either $N_{\rm H}$ or log (ξ) and the outflow velocity. On this basis, and given the degeneracies between $N_{\rm H}$ and log (ξ), the variability of the iron K absorption feature has been parametrized by either (i) allowing only the ionization to vary over the course of the observation with constant $N_{\rm H}$, or (ii) allowing only the column density to vary with constant log (ξ). In both scenarios, we kept the outflow velocity constant at (i) $v_{\rm w} = 0.25 \pm 0.01c$ and (ii) $v_{\rm w} = 0.24 \pm 0.01$c between the sequences for each case above.[4] In case (i) we find that the ionization of the line varies as $\log(\xi/{\rm erg\,cm\,s^{-1}}) = 6.6^{+0.9}_{-0.4}$, $\log(\xi/{\rm erg\,cm\,s^{-1}}) = 6.0^{+0.2}_{-0.3}$ and $\log(\xi/{\rm erg\,cm\,s^{-1}}) = 5.4^{+0.2}_{-0.3}$ in 2013a, 2013b and 2013c, respectively, by keeping the column density tied at $\log(N_{\rm H}/{\rm cm^2}) = 24.0^{+0.1}_{-0.3}$. In case (ii) the column density of the absorption line varies as $\log(N_{\rm H}/{\rm cm^{-2}}) = 23.1 \pm 0.2$, $\log(N_{\rm H}/{\rm cm^{-2}}) = 23.6^{+0.3}_{-0.1}$ and $\log(N_{\rm H}/{\rm cm^{-2}}) = 24.0 \pm 0.2$ in 2013a, 2013b and 2013c, respectively, for a constant ionization of $\log(\xi/{\rm erg\,cm\,s^{-1}}) = 5.3^{+0.3}_{-0.1}$. Further implications regarding the Fe K absorption variability will be discussed more in detail in Section 5.1 below, where the variations are investigated on a shorter time-scale across the *Suzaku* 2013 campaign by means of time-sliced spectroscopy.

5 TIME-SLICED SPECTRA

Fig. 7 shows the overall light curves of the 2013 *Suzaku* campaign, strongly indicating variability of the X-ray flux in PDS 456 on short time-scales. A prominent flare is detected, with the flux increasing by a factor of 4 between 400 and 450 ks in sequence 2013a, followed by smaller flares towards the second half of sequence 2013b. Guided by the visual properties of the overall light curve and softness ratio (between the 0.5–1 and 2–5 keV bands), the spectra were divided into a total of eight slices (see panel 1 in Fig. 7); this was done by taking into consideration the width of each slice and the number of counts in it. Note that for PDS 456, with $M_{\rm BH} \sim 10^9\,{\rm M}_\odot$, a variability time-scale of $\sim$100 ks corresponds to a light-crossing distance of $\sim$20 $R_{\rm g}$. A slice of at least 100 ks in duration was usually required for the 2013 spectra whilst, on the other hand, we had enough counts to isolate the much brighter flare between 400 and 450 ks into the observation. The plots of the fluxed νF_ν spectra and the Fe K band data to model ratios (obtained as in Fig. 2) of the eight slices are shown in the top and bottom panels of Fig. 8. The first four spectra (A–D), correspond to 2013a sequence, tracing the decline of an initial flare (A) followed by a quiescent period (B) together with the initial onset of the large flare (C) and the subsequent flare itself (D). In the remaining four spectra (E–H), corresponding to the 2013b and 2013c sequences, the Fe K absorption feature becomes very noticeable (E), progressing in strength (F) to reach maximum depth in slice G and tentatively recovering in slice H. The timing periods for each of the slices are noted in Table 4.

In Section 3.2, we used the `optxagnf` model to account for the optical/UV to hard X-ray SED of PDS 456. However, in order

[3] The ionization parameter is defined as $\xi = L_{\rm ion}/nR^2$, where $L_{\rm ion}$ is the 1–1000 Ryd luminosity, n is the electron density of the gas and R is the distance of the ionizing source from the absorbing clouds.

[4] The outflow velocity shows some variability during the observation in the range $v_{\rm w} \sim 0.23$–$0.27c$ (see Section 5). However, assuming a constant velocity is equivalent on statistical grounds.

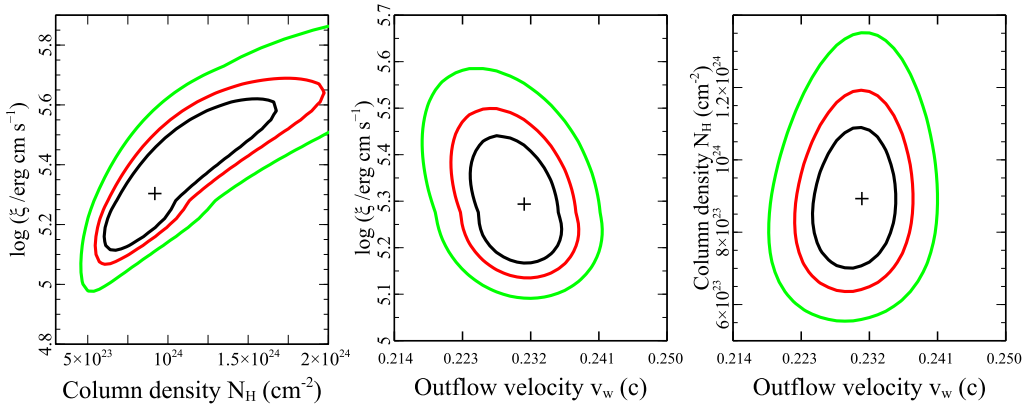

Figure 6. Two-dimensional contour plots from the XSTAR parameters of the highly ionized wind in the 2013c segment. The solid black, red and green lines correspond to 68, 90 and 99 per cent confidence levels for two interesting parameters, respectively. The elongated contour between the ionization against the column density parameters in the left-hand panel indicates a possible degeneracy. On the other hand, the other two contour plots (centre and right-hand panel) show no apparent degeneracies between either of the former parameters and the outflow velocity.

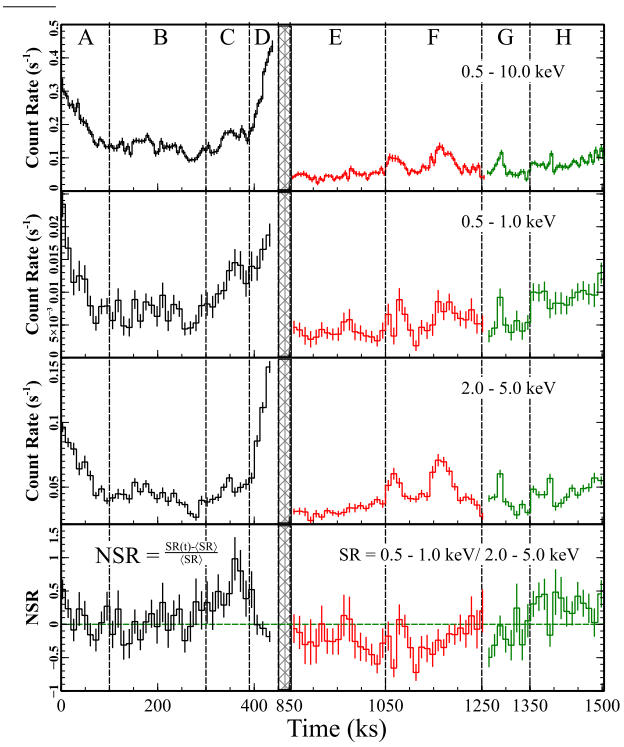

Figure 7. Light curves and normalized softness ratio (0.5–1/2–5 keV) for sequences 2013a (black), 2013b (red) and 2013c (green). The dashed vertical lines identify the boundaries of the eight slices.
Panel 1: XIS-FI (X-ray Imaging Spectrometer-Front Illuminated) 0.5–10.0 keV light curve of the overall *Suzaku* observation. Note the strong flare between 400 and 450 ks in segment D.
Panel 2: 0.5–1 keV soft band light curve.
Panel 3: 2–5 keV hard band light curve.
Panel 4: fractional change in the softness ratio (see the text for the definition). Positive (negative) values correspond to the softening (hardening) of the source with respect to the average spectral state. The bin size of the light curves are 5760 s, corresponding to one satellite orbit.

to describe the lower S/N time-sliced spectra over the 0.6–10 keV band, we used a simpler two-component model to provide a more convenient parametrization of the intrinsic continuum. We therefore parametrized the continuum with a phenomenological baseline model (hereafter MODEL I) of the form

$$\texttt{Tbabs} \times [\texttt{zpcfabs}_{\rm low} \times \texttt{zpcfabs}_{\rm high} \times (\texttt{po} + \texttt{bbody}) + \texttt{zgauss}_{\rm em} + \texttt{zgauss}_{\rm abs}], \quad (1)$$

where `Tbabs` accounts for the Galactic absorption using the cross-sections and ISM abundances of Wilms, Allen & McCray (2000). The Gaussian component $\texttt{zgauss}_{\rm em}$ parametrizes the ionized emission profile at 6.9 ± 0.1 keV (in the quasar rest frame). We note that this two-component (power law plus blackbody) continuum model, when applied to the parent sequences, is fully consistent with the earlier `optxagnf` findings. Again, the model requires two neutral partially covering absorbers, with column densities of $\log(N_{\rm H,low}/{\rm cm}^{-2}) = 22.3 \pm 0.1$ and $\log(N_{\rm H,high}/{\rm cm}^{-2}) = 23.2 \pm 0.1$. The soft excess, now parametrized with a blackbody (`bbody`), yields a temperature of kT $\sim 82^{+21}_{-20}$ eV, while the properties the Fe K emission and absorption profiles, as expected, are not modified compared to Table 3.

5.1 The Iron K short-term absorption variability

Here, we investigate the variability of the iron K absorption when applied to the short spectral slices. To provide an acceptable fit to the baseline continuum, we applied MODEL I introduced above over the 0.6–10 keV band. The high and low column covering fractions ($f_{\rm cov,low}$ and $f_{\rm cov,high}$) are allowed to vary between the eight slices, together with the power-law and blackbody normalizations. The high and low column densities of the partial covering absorbers were tied between the slices.

5.1.1 Gaussian modelling

To characterize the behaviour of the Fe K absorption line across all the eight slices, this has been initially parametrized using a simple Gaussian profile. Statistically speaking, we found that the Fe K absorption is not significant (at >99 per cent confidence level) in the first three slices (A–C). As the observation progresses the absorption feature becomes significant, through slices E ($\Delta\chi^2/\Delta\nu = 24/2$, equivalent to $\sim 5\sigma$ confidence level) and F ($\Delta\chi^2/\Delta\nu = 40/2$ $\sim 6\sigma$), reaching its maximum depth during slice G ($\Delta\chi^2/\Delta\nu = 77/2 > 8\sigma$), with EW $= -537^{+121}_{-131}$ eV, when the count rate becomes effectively null at the centroid of the absorption line ($E = 8.63 \pm 0.11$ keV; see

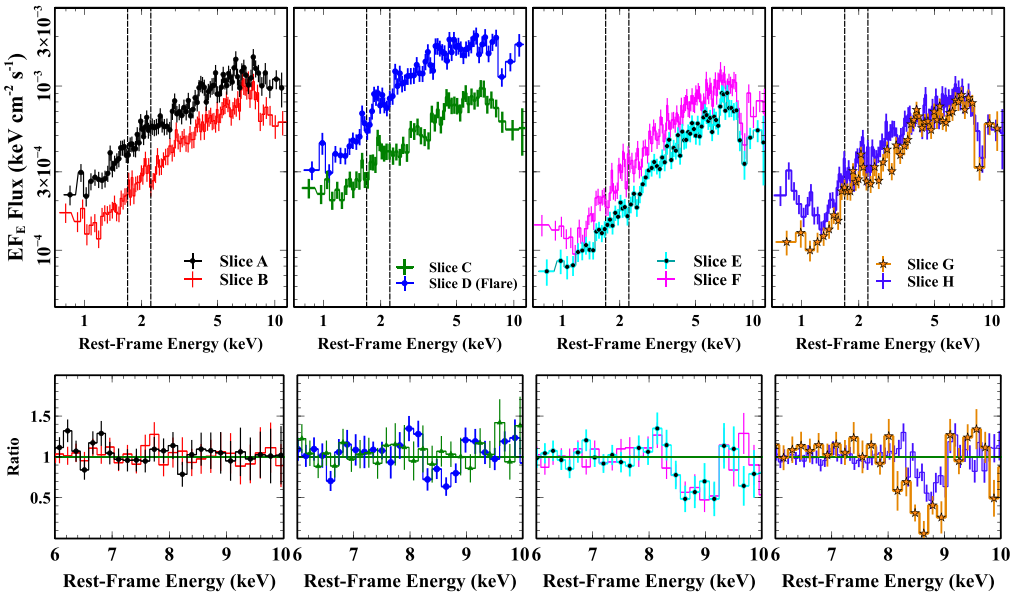

Figure 8. Top panels: fluxed spectra of the slices A (black), B (red), C (green), D (blue), E (cyan), F (magenta), G (orange) and H (violet). What is noticeable is the absence of a clear Fe K absorption feature in the first three spectra, and its possible onset in slice D (corresponding to the flare). The dotted rectangular areas represent the XIS Si edge calibration uncertainty range between 1.7 and 2.1 keV, ignored during fitting. The depth of the Fe K absorption feature (∼7.4 keV in the observed frame, ∼8.7 keV in the quasar rest frame) gradually increases after the flare between slice E and slice G, when the absorption trough becomes very prominent. The fluxed spectra have been plotted against a simple power law with $\Gamma = 2$ with minimum 50 cts per bin. Bottom Panels: ratio spectra of the slices in the Fe K band obtained as in Fig. 2.

Table 4. Model I – Fe K Gaussian absorption profile components for *Suzaku* XIS 2013 data. ^{t} denotes that the parameter is tied over the entire sequence 2013a (slices A–D).

Slice	Time	E (keV)^a	EW (eV)^b	$(\Delta\chi^2/\Delta\nu)^c$
A	0–100	8.55^t	<105	–
B	100–300	8.55^t	<156	–
C	300–400	8.55^t	<145	–
D	400–450	8.55 ± 0.15	254^{+116}_{-89}	15/2
E	850–1050	8.84 ± 0.14	341^{+112}_{-121}	24/2
F	1050–1250	$8.85^{+0.12}_{-0.11}$	350^{+100}_{-90}	40/2
G	1250–1350	8.63 ± 0.11	537^{+121}_{-131}	77/2
H	1350–1510	8.69 ± 0.11	396^{+99}_{-113}	46/2

^{a}Rest-frame energy of the Gaussian absorption line,
^{b}equivalent width for a constant width of $\sigma = 282^{+69}_{-56}$ eV,
^{c}change in $\Delta\chi^2/\Delta\nu$ when the Gaussian component modelling the iron K absorption profile is removed.

Fig. 8). Assuming a common velocity width between all the slices as in Section 4.1, we obtained $\sigma = 282^{+69}_{-56}$ eV, thus corresponding to a velocity dispersion of ∼9900 km s^{-1}. Model I provided a statistically very good fit to the slices, with $\chi^2_\nu = 1554/1681$. The parameter details of the Gaussian absorption line, for each of the eight slices, are listed in Table 4 and plotted in Fig. 9(a).

5.1.2 XSTAR *modelling*

We then replaced the Gaussian absorption line profile in Model I above with a multiplicative XSTAR absorption grid, generated as described earlier in Section 4 (hereafter this is referred to as Model II). Three scenarios were investigated to explain the iron K short-term variability, where: (i) the column density of the fully covering wind is allowed to vary, while the ionization parameter is tied between the slices; (ii) the ionization parameter of the fully covering wind is allowed to vary, while the column density is tied; (iii) the wind covering factor ($f_{\rm cov,Wind}$) is allowed to vary, while both column density and ionization are fixed across the whole observation. All the XSTAR parameters in modelling the Fe K absorption profile are summarized in Table 5.

Fig. 9(b) shows the column density variability, corresponding to case (i) above, by keeping the ionization constant between the slices at $\log(\xi/{\rm erg\,cm\,s^{-1}}) = 5.3^{+0.3}_{-0.1}$. Remarkably, when we compare two adjacent slices the variability is consistent within the errors, but overall the column density of the highly ionized wind increases by a factor of ∼10 as the observation progresses – i.e. from $\log(N_{\rm H}/{\rm cm^{-2}}) < 22.8$ in slice A to $\log(N_{\rm H}/{\rm cm^{-2}}) = 24.0 \pm 0.1$ in slice G. In case (ii), Fig. 9(c), with the column density tied between the slices at $\log(N_{\rm H}/{\rm cm^{-2}}) = 24.1 \pm 0.1$, we find that instead the ionization parameter of the wind decreases during the observation reaching its lowest value in slice H, $\log(\xi/{\rm erg\,cm\,s^{-1}}) = 5.2 \pm 0.1$, compared to a lower limit of $\log(\xi/{\rm erg\,cm\,s^{-1}}) > 6.5$ in slice A. Thus in this scenario the ionization varies by a factor of ∼10 or more between the two ends of the observation. In physical terms, however, for the ionization to follow such a trend, the ionizing flux has to vary by a factor of ∼10, unless the density and/or distance of the gas from the source also varies.[5] While both cases (i) and (ii) provided an excellent fit to the data, yielding $\chi^2_\nu = 1552/1685$ and $\chi^2_\nu = 1543/1682$, respectively, case (ii) appears to be physically ruled out, as such drastic ionization changes do not occur in response to similar changes of the hard X-ray continuum.

[5] This latter case is not easily distinguishable from a simple column density change, which is already considered in case (i).

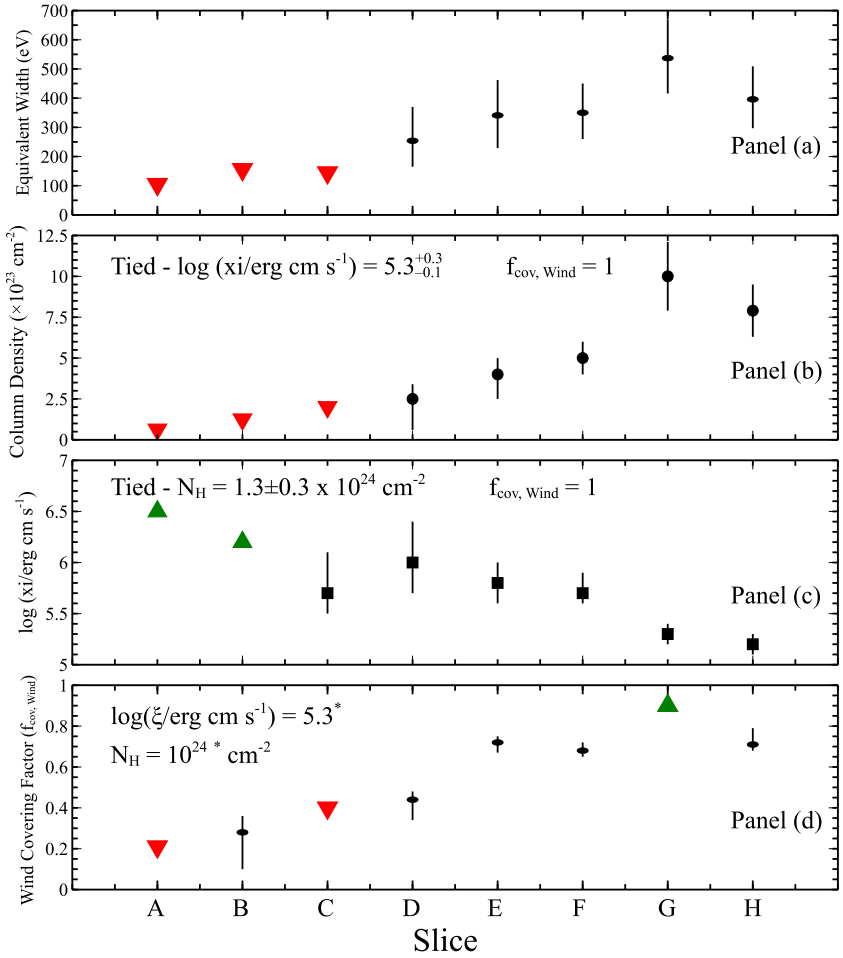

Figure 9. Fe K absorption short-term variability across the observation when modelled with either a Gaussian profile (panel a) or XSTAR (panels b–d). (a) EW evolution with time. (b) Column density variability assuming constant ionization and $f_{\rm cov,Wind} = 1$. (c) Ionization variability assuming constant column density and $f_{\rm cov,Wind} = 1$. (d) Variability of $f_{\rm cov,Wind}$ by assuming fixed ionization and column density.

Table 5. Model II – XSTAR photoionization model components of the Fe K absorption profile for *Suzaku* XIS 2013 data. * denotes that the parameter has being fixed, ^{t} denotes that the parameter is tied to the first segment value. The red triangles represent upper-bound measurements, while green triangles indicate lower-bound measurements. See the text for the details of the three different cases.

	A	B	C	D	E	F	G	H
				Case (i) $(\log(\xi/{\rm erg\,cm\,s^{-1}}) = 5.3^{+0.3}_{-0.1}), f_{\rm cov,Wind} = 1, v_{\rm w} = 0.245^{+0.003}_{-0.005}c$				
$\log(N_{\rm H}/{\rm cm^{-2}})$	<22.8	<23.1	<23.3	$23.4^{+0.2}_{-0.6}$	$23.6^{+0.1}_{-0.2}$	23.7 ± 0.1	24.0 ± 0.1	23.9 ± 0.1
				Case (ii) $(\log(N_{\rm H}/{\rm cm^{-2}}) = 24.1 \pm 0.1), f_{\rm cov,Wind} = 1, v_{\rm w} = 0.257^{+0.011}_{-0.010}c$				
$\log(\xi/{\rm erg\,cm\,s^{-1}})$	>6.5	>6.2	$5.7^{+0.4}_{-0.2}$	$6.0^{+0.4}_{-0.3}$	5.8 ± 0.2	$5.7^{+0.2}_{-0.1}$	5.3 ± 0.1	5.2 ± 0.1
				Case (iii) $(\log(N_{\rm H}/{\rm cm^{-2}}) = 24.0^*, \log(\xi/{\rm erg\,cm\,s^{-1}}) = 5.3^*)$				
Wind $f_{\rm cov}$	<0.21	$0.28^{+0.08}_{-0.18}$	<0.40	$0.44^{+0.04}_{-0.10}$	$0.72^{+0.03}_{-0.07}$	$0.68^{+0.04}_{-0.03}$	>0.89	$0.71^{+0.08}_{-0.03}$
$v_{\rm w}(c)$	0.24^t	0.24^t	0.24^t	0.24 ± 0.02	0.27 ± 0.02	0.27 ± 0.01	0.24 ± 0.01	0.25 ± 0.02

We explored case (iii) in Fig. 9(d) where, by assuming a fixed column density and ionization at $\log(N_{\rm H}/{\rm cm^{-2}}) = 24.0$ and $\log(\xi/{\rm erg\,cm\,s^{-1}}) = 5.3$, the variability of the absorption profile is instead accounted for by changes in the covering fraction of the iron K absorber. In this model, in order to compensate for the loss of flexibility as both $N_{\rm H}$ and $\log(\xi)$ are now constant, we also allowed the wind velocity to vary over the single slices. This better accounts for the moderate redwards shift of the line energy in the second part of the observation (see also Table 4). We find that the X-ray source is virtually unobscured in slice A (as the ionized absorber is covering <21 per cent), and as the observation progresses the gas moves across the line of sight almost fully covering the source in slice G (>89 per cent covering); by the end of the observation, the X-ray source may begin to uncover again in slice H (71^{+8}_{-3} per cent). Thus either $N_{\rm H}$ or $f_{\rm cov,Wind}$ changes may account for the variability of the iron K absorption feature. The physical implications will be examined in detail in the discussion.

Table 6. Model IIa parameters for *Suzaku* XIS 2013 slices. The spectral changes are accounted for by variability of the partial covering absorber. The blackbody and power-law normalizations are varying together through the same scale factor throughout the eight slices.

		Power law $\Gamma = 2.5 \pm 0.2$		bbody $kT = 69^{+24}_{-21}$ eV		$\mathbf{pc}_{low}$ $\log(N_{H,low}/cm^{-2})$ 22.3 ± 0.1	$\mathbf{pc}_{high}$ $\log(N_{H,high}/cm^{-2})$ 23.2 ± 0.1	Model statistic	
Slice	Time (ks)	$norm^a_{po}$	F^b_{2-10}	$norm^c_{bb}$	$F^d_{0.5-2}$	$f_{cov,low(per\,cent)}$	$f_{cov,high(per\,cent)}$	$(\chi^2/\nu)^e$	N.P.^{e}
A	0–100	$3.3^{+1.2}_{-0.8}$	2.3	6.0	0.33	75^{+4}_{-6}	59^{+6}_{-7}	218/224	0.59
B	100–300	$2.4^{+0.9}_{-0.5}$	1.6	4.3	0.18	78^{+4}_{-5}	66^{+5}_{-6}	241/255	0.73
C	300–400	$2.5^{+1.0}_{-0.6}$	1.8	4.6	0.28	72^{+5}_{-7}	60^{+7}_{-8}	139/143	0.58
D	400–450	$5.1^{+1.9}_{-1.1}$	3.9	9.1	0.41	85 ± 3	47^{+9}_{-11}	148/160	0.75
E	850–1050	$2.1^{+0.8}_{-0.5}$	1.3	3.8	0.10	82^{+4}_{-5}	72^{+4}_{-5}	168/193	0.90
F	1050–1250	$3.0^{+1.2}_{-0.7}$	1.9	5.4	0.14	84^{+3}_{-4}	69 ± 5	283/278	0.41
G	1250–1350	$2.2^{+0.9}_{-0.5}$	1.6	4.0	0.14	84^{+3}_{-4}	61^{+6}_{-8}	128/123	0.36
H	1350–1510	$2.4^{+0.9}_{-0.5}$	1.8	4.4	0.21	80^{+3}_{-4}	55^{+7}_{-8}	256/243	0.27
					$\chi^2/\nu = 1581/1689$				

[a]Power-law normalization, in units of 10^{-3} photons keV^{-1} cm^{-2} s^{-1} at 1 keV,
[b]observed (non-absorption corrected) power-law flux between 2 and 10 keV, in units of 10^{-12} erg cm^{-2} s^{-1},
[c]blackbody normalization in units of 10^{-4} (L_{39}/D^2_{10}), where L_{39} is source luminosity in units of 10^{39} erg s^{-1} and D_{10} is the distance to the source in units of 10 kpc,
[d]observed blackbody (soft excess) flux between 0.5 and 2 keV, in units of 10^{-12} erg cm^{-2} s^{-1},
[e]χ^2, degrees of freedom and null hypothesis probability (N.P.) calculated in each individual slice.

5.2 What causes the continuum short-term spectral variability?

In addition to the iron K absorption changes, the 2013 observations also show a significant broad-band continuum spectral variability. Fig. 7 (bottom panel) shows the normalized softness ratio (NSR), computed as the difference between the 0.5–1 keV over 2–5 keV softness ratio (as a function of time) and its mean value, divided by the mean itself. This was defined mathematically as $\mathrm{NSR} = \frac{\mathrm{SR(t)} - \langle \mathrm{SR} \rangle}{\langle \mathrm{SR} \rangle}$, and shows the fractional change in the softness ratio (see Fig. 7 lower panel). This can be seen in particular prior to and during the course of the flare (slices C and D). This variability can also be appreciated from the spectral shape of the individual slices plotted in Fig 8 (top panels).

In particular, we want to test whether the broad-band spectral variability is mainly produced by either (i) rapidly varying partial covering absorption or (ii) variations in the intrinsic shape of the continuum, such as the power law and soft excess, while the partial covering parameters (N_H, f_{cov}) are assumed to remain constant between the slices. We adopt MODEL II (including the XSTAR modelling of the iron K absorption) as our baseline continuum model to test both scenarios.

5.2.1 *Partial covering variability*

In this scenario, the X-ray photons are reprocessed due to the presence of compact clouds of gas, that partially absorb the AGN emission allowing a fraction $(1 - f_{cov})$ to emerge unattenuated. The size scale of these clouds is typically similar to the X-ray emitting region, of the order of a few tens of R_g (e.g. Risaliti et al. 2007). For simplicity, the column densities of the two required partial covering zones are not allowed to vary between the slices, so that the spectral changes over the course of the observation are only due to variations in the covering fractions. Note that we would obtain statistically equivalent results by letting the column densities, rather than the covering fractions, vary between the slices. The relative flux normalizations of the blackbody and the power-law continuum are *only* allowed to vary together by the same factor, i.e. we assumed that there is no intrinsic continuum spectral variability (hereafter Model IIa).

For the partial coverer, the column density of the two regions are found again to be $\log(N_{H,high}/cm^{-2}) = 23.2 \pm 0.1$ and $\log(N_{H,low}/cm^{-2}) = 22.3 \pm 0.1$. For the high column zone, the covering fraction reaches its minimum during the flare (slice D) at $f_{cov,high} = 0.47^{+0.09}_{-0.11}$, and increases to its maximum value $f_{cov,high} = 0.72^{+0.04}_{-0.05}$ in slice E. Thus slice D is the highest flux/least absorbed spectrum overall, while slice E is the lowest flux/most absorbed spectrum. Conversely, the variations in the covering fractions for the low column partial coverer are smaller, simply ranging from $f_{cov,low} = 0.72^{+0.05}_{-0.07}$ in slice C to $f_{cov,low} = 0.85 \pm 0.03$ in slice D (see Table 6).

This suggests that the high column covering fractions account for most of the spectral variability, and tend to vary of ± 15 per cent around the mean ($\sim$60 per cent) but never reaching zero. The range of variability of $f_{cov,high}$ can give us an idea of the possible number of clouds (N) crossing our line of sight at any time, as in first approximation it is related to $1/\sqrt{N}$. This suggests that a large number of clouds ($N \gtrsim 25$) are needed along the line of sight to produce small ($\sim$20 per cent) variations in covering. However, $N > 25$ would imply that the size of each cloud is $\sim 1\,R_g$, thus favouring an alternative scenario where the clouds are just a few but have an irregular or filamentary shape. The temperature of the blackbody component is $kT = 69^{+24}_{-21}$ eV, slightly lower but still consistent with the values previously obtained. Overall, the variable partial covering model provided an excellent fit to the data, with $\chi^2_\nu = 1581/1689$.

5.2.2 *Intrinsic spectral variability*

Alternatively, we tested if the main driver of the short-term spectral variability is actually a change in the intrinsic continuum via independently variable normalizations of the blackbody and power-law components. The partial covering fractions

Table 7. Model IIb parameters for *Suzaku* XIS 2013 slices for the intrinsic changes scenario. Here the power-law and blackbody components are allowed to vary independently, while $N_{\rm H}$ and $f_{\rm cov}$ are constant for both absorbers. The temperature of the blackbody component was fixed to the best value found in MODEL IIa, i.e. $kT = 69$ eV, in order to avoid physically unrealistically high values to model the curvature present at higher energies. All the quantities and units are the same as in Table 6. The last column shows the difference in χ^2 and degrees of freedom compared to Model IIa.

		Power law ($\Gamma = 2.5 \pm 0.1$)		bbody (kT=69 eV)			Model statistic	
Slice	Time (ks)	$\rm norm_{po}$	F_{2-10}	$\rm norm_{bb}$	$F_{0.5-2}$	(χ^2/ν)	N.P.	$(\Delta\chi^2/\Delta\nu)$
A	0–100	$3.6^{+1.2}_{-0.9}$	2.5	$9.5^{+4.5}_{-3.9}$	0.38	271/226	2.0×10^{-2}	53/2
B	100–300	$2.3^{+0.7}_{-0.6}$	1.6	$5.1^{+2.3}_{-2.9}$	0.21	244/257	7.2×10^{-1}	3/2
C	300–400	$2.8^{+0.9}_{-0.7}$	1.9	$17.0^{+7.1}_{-5.5}$	0.69	177/145	3.5×10^{-2}	38/2
D	400–450	$6.0^{+1.9}_{-1.5}$	4.1	<14.0	<0.25	170/162	3.0×10^{-1}	22/2
E	850–1050	$1.4^{+0.5}_{-0.4}$	1.1	<1.4	<0.06	224/195	7.9×10^{-2}	56/2
F	1050–1250	$2.5^{+0.8}_{-0.6}$	1.7	<3.6	<0.15	372/280	1.9×10^{-4}	89/2
G	1250–1350	$2.2^{+0.7}_{-0.6}$	1.5	<4.5	<0.18	133/125	3.0×10^{-1}	5/2
H	1350–1510	$2.6^{+0.8}_{-0.6}$	1.8	$13.0^{+4.9}_{-3.8}$	0.53	257/245	2.9×10^{-1}	1/2
				χ^2/ν =1848/1697				

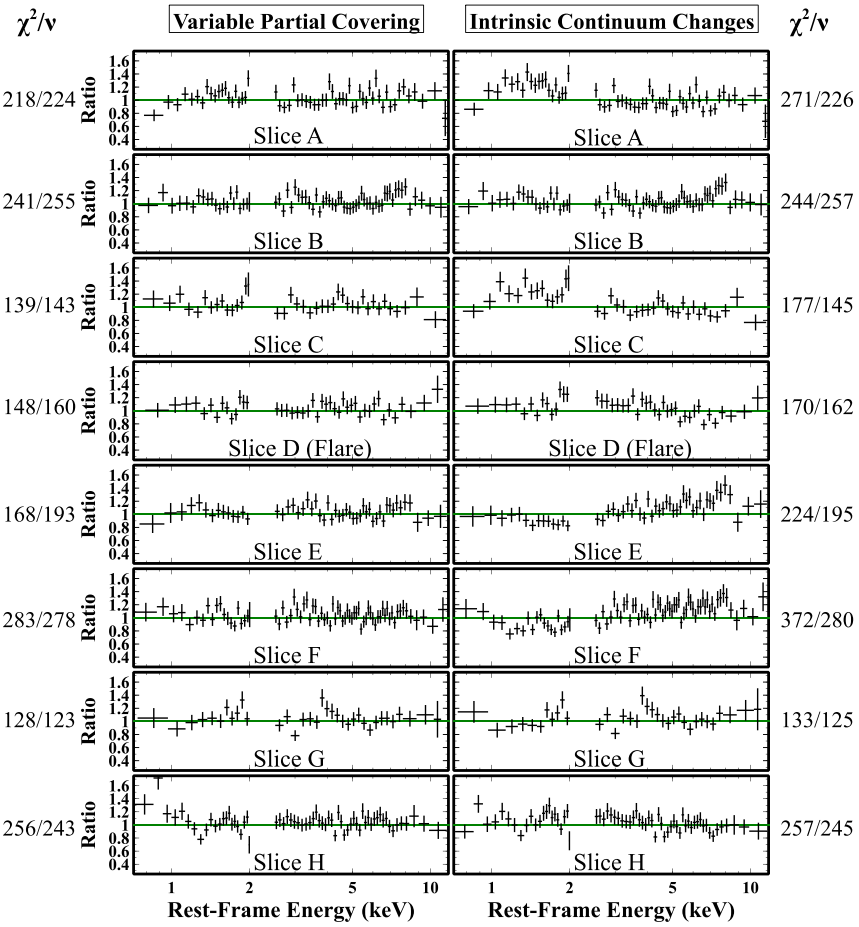

Figure 10. Plots comparing the residuals of each individual slice fitted with a variable partial covering model (left) or intrinsic spectral variability (right). Statistically speaking the χ^2/ν values of the variable partial covering model are equal or lower in all the eight slices compared to the intrinsic variability fit (see Tables 6 and 7). This is due to the extra curvature present in the residuals when the covering fraction is not allowed to vary.

$f_{\rm cov,low} = 81^{+3}_{-4}$ per cent and $f_{\rm cov,high} = 63^{+5}_{-6}$ per cent and column densities $\log(N_{\rm H,low}/{\rm cm}^{-2}) = 22.3 \pm 0.1$ and $\log(N_{\rm H,high}/{\rm cm}^{-2}) = 23.2 \pm 0.1$ are assumed to be constant between the slices (See Table 7). Notably, the values of both $f_{\rm cov,low}$ and $f_{\rm cov,high}$ are almost coincident with the average values found in the previous case. Statistically, this model (hereafter model IIb) gives an overall worse fit ($\chi^2/\nu = 1848/1697$) compared to the variable partial covering scenario, by $\Delta\chi^2/\Delta\nu \sim 270/8$. On this basis, we investigated these differences through the inspection of the residuals in each of the eight slices (see Fig. 10).

Generally speaking, when the partial covering absorption is constant the χ^2 is worse in all of the slices, in particular in some of the

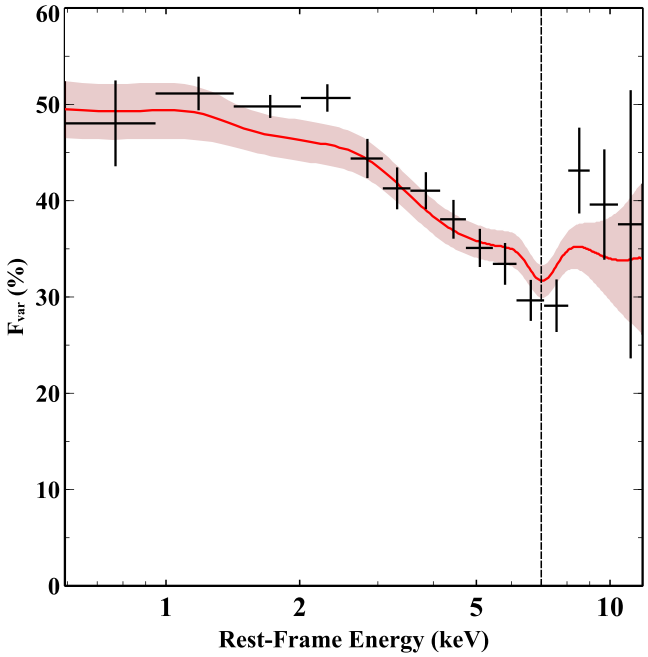

Figure 11. X-ray fractional variability from the 2013 *Suzaku* observations (in black). The iron K emission band centred at 7 keV (dashed black line) appears to be less variable than the rest of the spectrum. This may be associated with the reprocessed emission arising from the more distant material within the wind. The solid red line corresponds to the simulated F_{var} shape based on MODEL IIa (see text for details). The curve has been smoothed with a spline function, and the shaded area indicates the 1σ dispersion for 2000 mock light curves.

pre- and post-flare (e.g. C, E and F). Without allowing the absorber covering fractions to vary, there is in fact an additional curvature present in the residuals as shown in the right-hand panels of Fig. 10. Model IIb seems to account for some of the slices (i.e. slice B, G and H), although a caveat is that the blackbody normalizations are strongly varying between the slices (e.g. from slice C to E and from slice G to H) and not always in sync with the power law changes, possibly indicating that such extreme intrinsic changes are physically unrealistic (see Table 7 for values).

5.3 Fractional variability

In order to further quantify the spectral variability, we also calculated the fractional variability (F_{var}) in different energy bands, adopting a time binning of 5760 s (i.e. one *Suzaku* orbit) and using the method described in Vaughan et al. (2003). Qualitatively, the overall shape of the broad-band F_{var} spectrum (plotted in Fig. 11) appears broadly consistent with the results of either Model IIa (variable partial covering, Table 6) or Model IIb (intrinsic continuum changes, Table 7). Indeed if, the continuum were variable without any spectral variability, which would be the case if the power-law and soft excess components varied in proportion together, then the F_{var} spectrum would, in principle, appear to be constant across all energies. Here instead the variability in the softer band is enhanced with respect to the hard X-ray band. This behaviour could be naturally attributed to: (i) absorption variability seen as partial covering fraction changes across the observation and/or (ii) a two-component continuum, where the soft X-ray band component is more variable compared to the hard one. In either case, the soft X-rays would be more affected with respect to the harder X-rays, resulting in an enhanced F_{var} towards lower energies.

To quantitatively test the F_{var} spectrum against the actual spectral models, we simulated 2000 light curves based on the spectral parameters obtained for the slices from the previous section. We used as an input for the simulations the best-fitting spectral model of Table 6 (MODEL IIa), where the spectral variability is produced by the partial covering absorber. Informed by the best-fitting parameters from the individual spectral slices, the partial covering fractions ($f_{cov,low}$ and $f_{cov,high}$) were allowed to vary within the ranges from $0.70 < f_{cov,low} < 0.85$ and $0.4 < f_{cov,high} < 0.8$. The soft (blackbody) and hard X-ray (power-law) components of the continuum were allowed to vary together (as per MODEL IIa) by a factor of 0.5–2 in respect to the average normalization, which represents the expected range of intrinsic continuum variability (see Fig. 7). Each simulated light curve was then randomly generated by varying the spectral parameters within these ranges and the subsequent F_{var} calculated versus energy from averaging over all 2000 simulated curves.

The result is also shown in Fig. 11, where the red solid line corresponds to the simulated F_{var} model (and associated 1σ dispersion shown as the shaded area), compared to the actual F_{var} spectrum measured from the observations. The overall observed shape and normalization of the F_{var} spectrum is generally well reproduced by the simulations, with the variable partial covering model not only accounting for the rising shape of the F_{var} spectrum towards lower energies, but also for the overall curvature. In contrast, MODEL IIb, where the power-law and blackbody components were allowed to vary independently (with the partial covering absorption held constant), underpredicts the F_{var} spectrum in the 1–3 keV range. This is likely due to the fact that the soft X-ray blackbody component only adds sufficient variability below 1 keV and thus the simulated F_{var} spectrum is then flatter compared to the observations. Thus the overall shape of the F_{var} spectrum appears consistent with the variable partial covering scenario presented in the previous section.

Furthermore, looking at Fig. 11, there is a minimum in F_{var} in the 6.5–7.5 keV energy band, which is centred on the ionized Fe K emission. This may also suggest that the iron line is less variable compared to the continuum, or at least is not varying on the same short time-scale of the X-ray continuum (of the order of $\sim$100 ks). In this light, we investigated from the spectral slices whether the iron K emission line responded to the variability of the continuum. Two opposite scenarios were investigated; first, we kept the Fe K emission line flux fixed between the slices, then we let the emission line flux to vary in sync with the continuum, so that the line EW is constant. As indicated from the F_{var} spectrum, we can achieve a very good fit in the constant flux scenario. In the second case, a constant EW produced a significantly worse fit by $\Delta\chi^2/\Delta\nu = 100/8$, thus indicating that there is no apparent short time-scale correlation between the Fe K line and the continuum flux. These results imply that on $\lesssim$100 ks time-scales the iron K emission is less variable than the continuum; this suggests that the iron K emitting region is larger than the typical continuum size inferred, which is of the order of $\sim$6–20 R_g (see below). The line may then originate from the outer regions of the disc or, alternatively, if it is associated with the wind as suggested by N15, its lack of variability would be consistent with an origin at distances $\gtrsim$100 R_g from the black hole.

We finally note that, after the iron K emission, the observed variability reaches again a larger value $F_{var} \sim 45$ per cent value between 8 and 9 keV, coincident with the energy of the iron K absorption

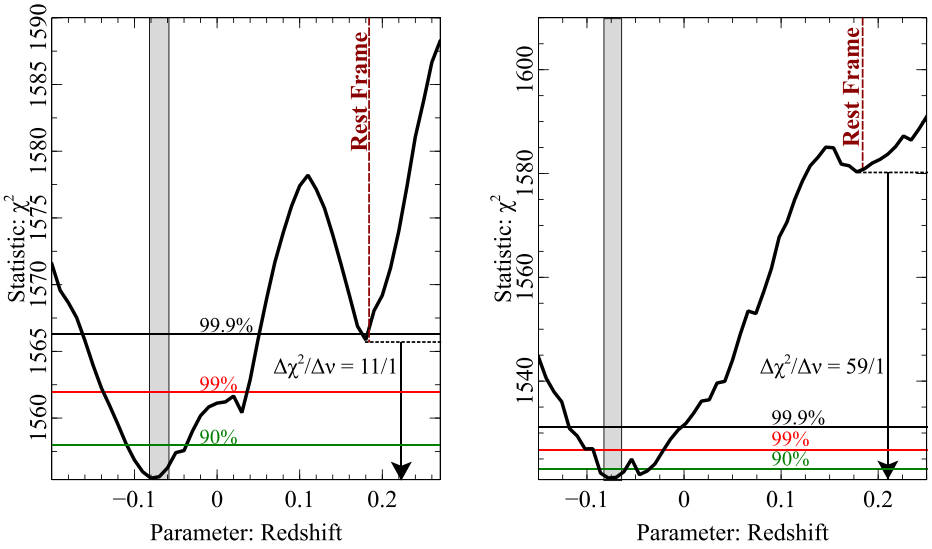

Figure 12. Left: contour plot of the χ^2 against the partial covering redshift parameter (used as proxy for the velocity) in all the slices. A local minimum at about the quasar rest frame (i.e. $z = 0.184$) is clearly visible, but the global minimum indicates that the partial covering layers are possibly outflowing with velocity comparable to that of the fully covering ionized wind, i.e. $v_{\rm pc} \sim v_{\rm w} \sim 0.25\,c$. This suggests that the two partially covering zones may correspond to the less ionized component of the same ultrafast wind. Right: as for left-hand panel, but with a mildly ionized partial covering absorber. The global minimum corresponds to a statistical improvement, with respect to the rest-frame velocity, of $\Delta\chi^2/\Delta\nu = 59/1$. The vertical shaded area correspond to the range of $v_{\rm w}$ across the slices given in Table 5.

feature. This suggests that the iron K absorption variability, discussed earlier in Section 5.1, may be responsible for this increase in $F_{\rm var}$. For simplicity, however the properties of the highly ionized wind were not allowed to vary when generating the simulated light curves.

5.4 Properties of the partial covering absorber

From the previous sections, we conclude that we cannot explain the overall short-term spectral variability without invoking a variable partial coverer. Therefore there is a natural question of what the partial covering is associated with.

One possibility is that it is the less ionized and more dense (or clumpy) part of the outflow. To test this, we investigated the outflow velocity of the partial covering absorber(s) ($v_{\rm pc}$) by allowing it to vary independently from the wind's outflow velocity ($v_{\rm w}$). The resulting fit (applied to the eight slices) suggested that this component is indeed outflowing with a velocity comparable to the velocity of the highly ionized gas. Fig. 12 (left) shows the contour plot of the χ^2 against the partial covering redshift parameter tied between all the slices (but allowing the other spectral parameters to vary). A local minimum at about the quasar's rest frame (i.e. $z = 0.184$) is clearly visible, however by assuming a systemic velocity for the partial coverer the fit statistic is worse by $\Delta\chi^2/\Delta\nu = 11/1$ compared to the best-fitting case. The global minimum in Fig. 12 indicates that the partial covering gas prefers an outflow velocity of $v_{\rm pc} \sim 0.25\,c$ over a null velocity at the $\sigma = 3.29$ (99.9 per cent) confidence level. This indicates that the two partially covering zones might be the least ionized component of the *same* fast ($v_{\rm pc} \sim v_{\rm w} \sim 0.25\,c$) wind.

As a consistency check, we also tested the above result by replacing the two neutral partial covering components with two mildly ionized absorbers, modelled through the same absorption grid responsible for the absorption line at Fe K.

We therefore constructed MODEL III expressed as

$$\begin{aligned}&\texttt{Tbabs} \times \texttt{xstar}_{\rm Fe} \times \{[(C_{\rm high} \times \texttt{xstar}_{\rm pc,high})\\ &\quad + (C_{\rm low} \times \texttt{xstar}_{\rm pc,low}) + (1 - C_{\rm high} - C_{\rm low})]\\ &\quad \times \texttt{po} + \texttt{bbody} + \texttt{zgauss}\},\end{aligned} \tag{2}$$

where $C_{\rm high}$ and $C_{\rm low}$ are multiplicative constants of value <1, $\texttt{xstar}_{\rm Fe}$ represents the fully covering highly ionized wind, while $\texttt{xstar}_{\rm pc,low}$ and $\texttt{xstar}_{\rm pc,high}$ represent the low and high column, mildly ionized partial covering zones, respectively. The Gaussian component `zgauss` again parametrizes the ionized emission profile, while the soft excess is described by the `bbody` component. Note that the model structure is slightly different compared to either Model I or Model II, so that $C_{\rm high}$ and $C_{\rm low}$ are not immediately comparable to the previous $f_{\rm cov,high}$ and $f_{\rm cov,low}$. Here the constants $C_{\rm high}$ and $C_{\rm low}$ physically represent the mutual covering fractions of the high and low column absorbers, so that the remaining fraction $1 - C_{\rm high} - C_{\rm low}$ of the continuum is not absorbed by either layer and passes through the partial coverer unattenuated. Also, for simplicity, the blackbody component is assumed to be unobscured. For this reason, its temperature is somewhat larger ($kT = 110^{+8}_{-11}$ eV).[6]

Overall, the column densities $\log(N_{\rm H,high}/{\rm cm}^{-2}) = 23.6^{+0.3}_{-0.4}$ and $\log(N_{\rm H,low}/{\rm cm}^{-2}) = 22.5 \pm 0.3$ are marginally larger (but fully consistent) than in the neutral absorber case, as the gas here is more transparent to the illuminating radiation. We get $\log(\xi/{\rm erg\,cm\,s^{-1}}) = 2.5 \pm 0.2$ for the high column partial coverer and $\log(\xi/{\rm erg\,cm\,s^{-1}}) = 0.62^{+0.18}_{-0.08}$ for the low column one. Notably, the high column zone is confirmed to be the main source of the observed continuum variability, and its behaviour is very similar to the one previously described, ranging from ∼50 per cent (slice D)

[6] However, by letting the blackbody component vary together with the power law and experience exactly the same absorption, we still achieve a very good fit ($\chi^2_\nu \simeq 0.94$) and the results do not change.

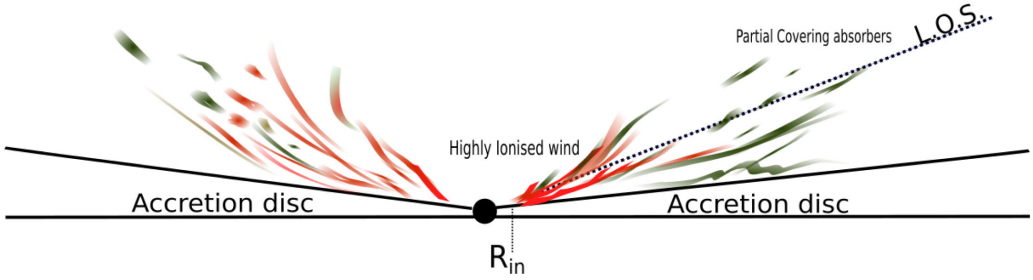

Figure 13. A schematic representation of a possible structure of the outflow and the relative locations of the highly ionized wind (red) and less ionized partial covering absorbers (green) within the outflow. The dashed line represents a possible line of sight. The highly ionized absorber is located in the vicinity of the black hole whilst the less ionized partial covering material is possibly situated further out, both being part of the same outflow.

to ∼80 per cent (slice E). The fraction of the intrinsic continuum that is not affected by any absorber (apart from the fully covering highly ionized one) is always of the order of a few per cent, and never exceeds 10 per cent.

The confidence contour plotted in Fig. 12 (right) suggests a very similar behaviour in χ^2 space for the velocity of the partial coverer. Indeed, the statistical improvement with respect to a systemic velocity is much larger ($\Delta\chi^2/\Delta\nu = 59/1$). Thus we conclude that the partial covering absorbers' outflow velocity, $v_{\rm pc} = 0.25^{+0.01}_{-0.05}\,c$, is consistent with that of the iron K absorber.

6 DISCUSSION

In the previous section, we found that the observed short-term spectral variability can be explained by the combination of partial covering absorption and intrinsic continuum variability, although the former effect may be the dominant cause in this observation. Furthermore, by investigating in more detail the properties of the partial covering absorbers, we found that their outflow velocity is comparable to that of the highly ionized wind (i.e. $v_{\rm pc} \sim v_{\rm w} \sim 0.25\,c$) for both the neutral and mildly ionized case. This suggests that the partial covering may be the less ionized but clumpier component of the disc wind, as also supported by the analysis of the soft X-ray absorption features in the high resolution grating *XMM–Newton*/RGS spectra (Reeves et al. 2016). A schematic representation of the possible location and structure of the highly ionized wind and partial covering absorbers in context of the outflowing material from the accreting supermassive black hole is shown in Fig. 13.

6.1 Properties of the clumpy wind and constraints on the X-ray emitting region

During the observation, the column density $N_{\rm H}$, or equivalently the EW of the Fe K absorption feature, increased by a factor of ∼10, from $\log(N_{\rm H}/{\rm cm}^{-2}) < 22.8$ in slice A to $\log(N_{\rm H}/{\rm cm}^{-2}) = 24.0^{+0.1}_{-0.3}$ in slice G. Alternatively, these variations may be accounted for by a change in the wind covering factor ($f_{\rm cov,Wind}$), where initially the absorber is not covering the X-ray source but progresses to almost fully covering (>89 per cent) at the time of slice G. These changes could be caused by the transit of a cloud or stream of highly ionized material moving across the line of sight as part of an inhomogeneous outflow (see Fig. 9d). The linear size of the transiting clump can be estimated as $\Delta R_{\rm c} \sim v_{\rm w}\Delta t$, assuming that the transverse (Keplerian) velocity is comparable to the outflow velocity (i.e. $v_{\rm K} \sim v_{\rm w}$), and that $\Delta R_{\rm c}$ is similar to the size of the X-ray source. The putative cloud, in fact, cannot be much smaller than the X-ray emitting region in PDS 456 since an almost complete covering is reached in slice G (see Fig. 8 bottom panel). At the same time it cannot even be much larger, given that in slice H the covering seems to decrease instead of remaining close to $f_{\rm cov,Wind} \sim 1$. We choose $\Delta t = 400$ ks, corresponding to the time between the initial (statistically significant, ∼3σ) onset of the absorption profile in slice E and its completion at maximum depth in slice G (>5σ). By adopting $v_{\rm w} \simeq 0.25\,c$, we estimate $\Delta R_{\rm c} \approx 3 \times 10^{15}$ cm ∼20$R_{\rm g}$ for $M_{\rm BH} \sim 10^9\,{\rm M}_\odot$. This can also be seen as a constraint on the size of the X-ray emitting region, which therefore cannot be larger than ∼20 $R_{\rm g}$ in order for the absorber to reach full covering during slice G.

For an ionizing luminosity of $L_{\rm ion} \sim 5 \times 10^{46}\,{\rm erg\,s^{-1}}$, and taking the average column density between slices E and H of $\log(N_{\rm H}/{\rm cm}^{-2}) \sim 24$, as well as the average ionization parameter of $\log(\xi/{\rm erg\,cm\,s^{-1}}) \sim 5.3$, the distance of the absorber from the ionizing continuum can be estimated. Considering an average hydrogen number density of $n_{\rm H} \sim N_{\rm H}/\Delta R \sim 3.3 \times 10^8\ {\rm cm}^{-3}$, then from the definition of the ionization parameter $R = (L_{\rm ion}/n_{\rm H}\xi)^{1/2} \sim 2.8 \times 10^{16}$ cm, or $R \sim 180\ R_{\rm g}$. This radial estimate is of the same order of that measured by N15. These results suggest that we are viewing through a clumpy wind at typical distance of few 100 $R_{\rm g}$ from the black hole.

6.1.1 *Estimate of the wind radial distance from its Keplerian velocity*

Above, in estimating the radial distance of the wind from the black hole, we assumed that $v_{\rm K} \sim v_{\rm w}$. Relaxing this assumption, we now instead express the Keplerian velocity as $v_{\rm K}^2 = \frac{c^2}{r_{\rm g}}$, where $r_{\rm g} = \frac{R}{R_{\rm g}}$ is the distance in units of gravitational radii.

The hydrogen number density in terms of $r_{\rm g}$ is expressed as

$$n_{\rm H} \sim \frac{\Delta N_{\rm H}}{\Delta R_{\rm c}} \sim \frac{\Delta N_{\rm H}}{\Delta R_{\rm x}} \sim \frac{\Delta N_{\rm H} r_{\rm g}^{1/2}}{c\Delta t}, \quad (3)$$

where $\Delta R_{\rm x}$ is the size of the X-ray source. As we practically observe an eclipsing event of the X-ray source, we again assume that $\Delta R_{\rm x} \sim \Delta R_{\rm c}$ (Risaliti et al. 2007). $\Delta N_{\rm H}$ is the change in column density between slices E and H of the passing clump as shown in Fig. 9b. $\Delta R_{\rm c} = c\Delta t/r_{\rm g}^{1/2}$ is the transverse radial distance covered by the passing clump between slices E–H.

By substituting the definition of the ionization parameter we can therefore obtain an expression for the radial distance as

$$r_{\rm g}^{5/2} = \frac{L_{\rm ion}}{\xi}\frac{\Delta t c^5}{\Delta N_{\rm H}}(GM_{\rm BH})^{-2}. \quad (4)$$

From the known variables then $R \sim 3 \times 10^{16}$ cm $\sim 200\,R_{\rm g}$, which is of the same order of the previous estimate. The fast variability likely implies that the wind is not uniform but inhomogeneous. What we see in this observation may be therefore described as a $\sim$20 d long 'picture' of a complex time-dependent AGN accretion disc wind (Proga, Stone & Kallman 2000; Proga & Kallman 2004), where the line of sight absorption varies over a time-scale of days–weeks. On the other hand, G14 investigated whether the increase in depth of the Fe K absorption profile could be attributed to changes in the ionization state due to recombination within a smooth (constant column density over time) outflow in photoionization equilibrium. In this case, the estimate of the radial extent of the outflow was found to be $R \sim 1000\,R_{\rm g}$. Note, however, that a smooth wind without denser clumps would require another explanation to account for the variable partial covering.

6.2 Origin and energetics of the flare

In order to analyse the remarkable flare, we focused on the soft (0.5–1 keV) and the hard (2–5 keV) light curves corresponding to the first 450 ks of the observation (sequence 2013a, slices A–D). These are, respectively, plotted in panels 2 and 3 in Fig. 7 together with the corresponding softness ratio 0.5–1/2–5 keV (panel 4). Here, we observe a steady increase of the soft X-ray flux by a factor of $\sim$4 between $t \sim 250$ and 430 ks. In contrast, the hard X-ray flux shows a sharp increase, by a factor $\sim$3, between $t \sim 390$ and 430 ks. Therefore the doubling time for the soft flux is $\sim$90 ks, whilst the doubling time for the hard flux is $\sim$2–3 times shorter, implying from the light-crossing time argument that the approximate extent of the soft and hard X-ray emission regions in PDS 456 is $\sim$15–20$R_{\rm g}$ and $\sim$6–8 $R_{\rm g}$, respectively. This suggests a corona characterized by an extended region of 'warm' electrons combined with a more compact region of 'hot' electrons contributing to the rapid hard flare. This would overall be consistent with the earlier representation with the `optxagnf` disc plus corona model (see Section 3.2). As we do not have any information just after the flare (i.e. from $t = 450$–850 ks), at this stage we can only provide a speculative interpretation of the possible geometrical relation between the hot and warm coronae. We may either have (i) a layered coronal structure or (ii) a compact hot corona embedded into the warm one. The first case may produce a lag, and cannot be completely ruled out as we are unable to observe the peaks of the hard and soft light curves due to the scheduling gap (see Fig. 7). In the second case, the simultaneous rise of the soft and hard light curves may be interpreted as an accretion rate fluctuation (e.g. Arévalo & Uttley 2006) with consequent increase of seed disc photons; when the hot corona perceives the increase of the soft X-ray photon density, the observed slope of the hard X-ray light curve significantly steepens. Whatever the physical explanation, this is interestingly consistent with the most recent results from microlensing studies, which hint at soft and hard X-ray coronal components of different size (Mosquera et al. 2013).

One open question involves the origin of the flare itself. A possible scenario is whether the observed flare (in slice D) can be simply due to a 'hole' in the partial coverer, rather than to an intrinsically variable X-ray continuum. On this basis, we tested a model where *only* the covering fractions $f_{\rm cov,low}$ and $f_{\rm cov,high}$ were allowed to vary between the eight slices, whereas the normalizations of blackbody and power-law components were not. The overall fit statistic was substantially worse, $\Delta\chi^2/\Delta\nu = 333/14$, in the case where no intrinsic continuum variations were allowed. Thus it is likely that the flare is produced intrinsically.

6.2.1 *Can the flare drive the outflow?*

Another question arising is whether the strong flare emission could radiatively power the outflow in the latter part of the observation, as the outflow at iron K is more clearly detected after the occurrence of the flare in the light curve. From the transfer of photon momentum to the wind it follows that

$$\dot{p}_{\rm w} = \dot{M}_{\rm w} v_{\rm w} \sim \tau \frac{L_{\rm flare}}{c}, \tag{5}$$

where $\dot{p}_{\rm w}$, $\dot{M}_{\rm w}$ and $v_{\rm w}$ are the momentum rate, mass outflow rate and outflow velocity of the wind, while the Thomson depth is $\tau \sim 1$ for $N_{\rm H} \sim 10^{24}{\rm cm}^{-2}$, as observed in the highly ionized wind.

Thus the kinetic power (luminosity) of the wind is

$$\dot{E}_{\rm w} = \frac{1}{2}\dot{M}_{\rm w} v_{\rm w}^2 \sim \left(\frac{v_{\rm w}}{2c}\right) L_{\rm flare}, \tag{6}$$

or, integrating over time for the total energy:

$$E_{\rm w} \sim \left(\frac{v_{\rm w}}{2c}\right) E_{\rm flare}. \tag{7}$$

For an outflow velocity of $v_{\rm w} \sim 0.25\,c$, then $\dot{E}_{\rm w} \sim \dot{E}_{\rm flare}/8$, hence implying that we would expect only $\sim$10–15 per cent of the radiative power in the flare to be directly transferred to the wind.

From the best fit to the eight slices, we estimated the 1–1000 Ryd luminosity of the flare to be $L_{\rm Flare} \sim 2 \times 10^{46}$ erg s^{-1}.

Now, the mass outflow rate of the wind is given by

$$\dot{M}_{\rm w} \sim \Omega m_{\rm p} N_{\rm H} v_{\rm w} R_{\rm in}, \tag{8}$$

and based on the discussion in the previous sections we have adopted the following variables: $\Omega \sim 2\pi$ sr for the solid angle as deduced by N15, the average column density between slices E and H $N_{\rm H} > 5 \times 10^{23}$ cm^{-2}, $v_{\rm w} \sim 0.25\,c$ and $R_{\rm in} > 100\,R_{\rm g} \sim 1.5 \times 10^{16}$ cm. Hence we estimated $\dot{M}_{\rm w} \gtrsim 9\,M_{\odot}$ yr^{-1} $\sim 0.4\dot{M}_{\rm edd}$ (in good agreement with N15). The kinetic luminosity of the outflow is $\gtrsim 1.5 \times 10^{46}$ erg s^{-1}, or $\sim$0.1 $L_{\rm Edd}$ for $M_{\rm BH} = 10^9\,{\rm M}_{\odot}$.

The duration of the wind in slices E to H is at least $\sim$600 ks, thus the mechanical energy carried by the wind is at least $\sim 10^{52}$ ergs. To be conservative, we can assume that the flare is symmetric and persists at its maximum observed luminosity ($L_{\rm Flare} \sim 2 \times 10^{46}$ erg s^{-1}) for the entire duration of the observational gap, i.e. for 450 ks in total. This would impart a total radiative energy of up to $\sim 10^{52}$ erg. Indeed, this value represents a maximum upper limit for the total energy radiated during the flare as: (i) it is assumed that the full band 1–1000 Ryd ionizing luminosity has risen in proportion to the X-ray luminosity, which is unlikely be the case; (ii) the flare luminosity is assumed to remain constant for an extended period, contrary to the usual flaring behaviour. Thus the energy radiated during the flare may be an order of magnitude lower if the flare is short lived, which is likely given its rapid rise during slice D. Even for this maximum case, however, given that only $\sim$10–15 per cent of the radiative energy is deposited in the wind, it is not possible for the subsequent outflow to be purely driven by the radiation pressure provided by the flare alone. The discrepancy between the observed wind kinetic power and the estimated flare contribution is at least an order of magnitude, and probably even larger. Magnetically driven outflows may instead provide an alternative mechanism for the initial driving for such a powerful wind (e.g. Ohsuga et al. 2009; Fukumura et al. 2010, 2015; Ohsuga & Mineshige 2011; Kazanas et al. 2012). Alternatively the increased opacity through line driving may also be important in PDS 456 (Hagino et al. 2015).

7 CONCLUSIONS

In this paper, we have presented the results from the *Suzaku* observing campaign of the nearby luminous quasar PDS 456 carried out in early 2013 ($\sim$1 Ms total duration). We investigated the broad-band continuum by constructing an SED including the OM and *NuSTAR* spectra from the simultaneous *XMM–Newton* /*NuSTAR* campaign in 2013/14. As a result, a physically motivated accretion disc/X-ray corona model like `optxagnf` was able to account for the optical/UV to X-ray brightness ratio with sensible values of the accretion rate, $\log(L/L_{Edd}) \sim -0.1$ and coronal size, $\sim$10–40 R_g. However, this broad-band model alone could not account for the spectral curvature present in the low-flux 2013 *Suzaku* spectra. We show that partial covering absorption is required, and then investigated its variability over the course of the observation. The short-term spectral changes in PDS 456 were interpreted in terms of variable partial covering absorption and/or changes in the intrinsic continuum.

In the first scenario, we have found that the spectral variability on $\sim$100 ks time-scales may be due to neutral (or mildly ionized) clouds of gas that partially obscure the X-ray source while crossing the line of sight. Statistically speaking, the variable absorber model produces an excellent fit to the data ($\chi^2/\nu = 1581/1689$). Alternatively, we tested whether the spectral variability can be explained by variations in the intrinsic continuum only, where the partial covering absorbers (still required) are constant throughout the observation. While this model seems to account for some parts of the observation, it fails to account for the spectral variability in particular before and after a prominent flare, during which the flux rises by a factor of $\sim$4 in just $\sim$50 ks. In general, we cannot explain the overall short-term behaviour of PDS 456 without invoking a variable partial coverer combined, to a certain extent, with an intrinsically variable continuum.

On this basis we have investigated in more detail the properties of the partial covering absorbers. At least two layers of absorbing gas are required, of column density $\log(N_{H,low}/cm^{-2}) = 22.3 \pm 0.1$ and $\log(N_{H,high}/cm^{-2}) = 23.2 \pm 0.1$, with average line of sight covering factors of $\sim$80 per cent (with typical $\sim$5 per cent variations) and 60 per cent ($\pm$10–15 per cent), respectively. We have also found that these absorbers may be the least ionized component of the fast wind detected through the Fe XXVI K absorption feature, with typical outflow velocity of $\sim 0.25\,c$. We have shown that the short-term variability of the iron K absorption may be attributed to the line of sight variations in the column density (or covering fraction in an X-ray eclipse scenario). Through this variability, the size of the absorber is constrained to be $\sim 20\,R_g$. Following an almost complete obscuration event in the second half of the observation, also the size of the X-ray emitting region cannot be larger than this value. In addition to this, we estimated the typical radial distance of the high ionization absorber from the black hole to be of the order of $\sim 200\,R_g$.

We finally analysed the behaviour of the soft (0.5–1 keV) and hard (2–5 keV) band light curves during the course of the flare. From the doubling time in flux observed in both the soft and hard band, the X-ray emitting corona may be characterized by a 'warm', extended soft X-ray region of $\sim$15–20 R_g, which also includes a more compact ($\sim$6–8 R_g) zone of 'hot' electrons, responsible for the rapid rise in the 2–5 keV light curve. We ruled out that the flaring behaviour is instead due to a sudden 'hole' in the inhomogeneous absorber surrounding the X-ray source.

We have explored whether the radiation pressure imparted by the flare could deposit enough kinetic power in the outflowing material to drive the wind. The estimated radiative power of the flare was less than the mechanical power measured for the outflow by at least one order of magnitude, leading to the conclusion that another physical launching mechanism (e.g. magnetohydrodynamic) is likely contributing as well.

Finally, we calculated the fractional variability in the 2013 data set as a function of energy. We found that the iron K emission band is somewhat less variable than the rest of the continuum. This suggests that the iron K emission occurs from a much larger region than the continuum. This is consistent with the feature arising from size scales $\gtrsim 100\,R_g$, i.e. within the wind itself.

ACKNOWLEDGEMENTS

We thank the anonymous referee for their careful report, which helped us improving the clarity of the paper. This research has made use of data obtained from the *Suzaku* satellite, a collaborative mission between the space agencies of Japan (JAXA) and the USA (NASA). GM, JR, EN, MC and JG all acknowledge the financial support of STFC. VB acknowledges the support from the grant ASI-INAF NuSTAR I/037/12/0.

REFERENCES

Arévalo P., Uttley P., 2006, MNRAS, 367, 801
Arnaud K. A., 1996, in Jacoby G. H., Barnes J., eds, ASP Conf. Ser. Vol. 101, Astronomical Data Analysis Software and Systems V. Astron. Soc. Pac., San Francisco, p. 17
Bautista M. A., Kallman T. R., 2001, ApJS, 134, 139
Behar E., Kaspi S., Reeves J., Turner T. J., Mushotzky R., O'Brien P. T., 2010, ApJ, 712, 26
Blustin A. J., Page M. J., Fuerst S. V., Branduardi-Raymont G., Ashton C. E., 2005, A&A, 431, 111
Chartas G., Brandt W. N., Gallagher S. C., Garmire G. P., 2002, ApJ, 579, 169
Chartas G., Brandt W. N., Gallagher S. C., 2003, ApJ, 595, 85
Di Matteo T., Springel V., Hernquist L., 2005, Nature, 433, 604
Done C., Davis S. W., Jin C., Blaes O., Ward M., 2012, MNRAS, 420, 1848
Fabian A. C. et al., 2002, MNRAS, 335, L1
Fabian A. C. et al., 2012, MNRAS, 419, 116
Ferrarese L., Merritt D., 2000, ApJ, 539, L9
Fukumura K., Kazanas D., Contopoulos I., Behar E., 2010, ApJ, 715, 636
Fukumura K., Tombesi F., Kazanas D., Shrader C., Behar E., Contopoulos I., 2015, ApJ, 805, 17
Gallo L. C. et al., 2013, MNRAS, 428, 1191
Gebhardt K. et al., 2000, ApJ, 539, L13
Gofford J., Reeves J. N., Tombesi F., Braito V., Turner T. J., Miller L., Cappi M., 2013, MNRAS, 430, 60
Gofford J. et al., 2014, ApJ, 784, 77 (G14)
Green A. R., McHardy I. M., Lehto H. J., 1993, MNRAS, 265, 664
Haardt F., Maraschi L., 1991, ApJ, 380, L51
Haardt F., Maraschi L., 1993, ApJ, 413, 507
Hagino K., Odaka H., Done C., Gandhi P., Watanabe S., Sako M., Takahashi T., 2015, MNRAS, 446, 663
Hopkins P. F., Elvis M., 2010, MNRAS, 401, 7
Kaastra J. S., Mewe R., Liedahl D. A., Komossa S., Brinkman A. C., 2000, A&A, 354, L83
Kazanas D., Fukumura K., Behar E., Contopoulos I., Shrader C., 2012, Astron. Rev., 7, 92
King A., 2003, ApJ, 596, L27
King A. R., 2010, MNRAS, 402, 1516
King A. R., Pounds K. A., 2003, MNRAS, 345, 657
Koyama K. et al., 2007, PASJ, 59, 23
McKernan B., Yaqoob T., Reynolds C. S., 2007, MNRAS, 379, 1359
McQuillin R. C., McLaughlin D. E., 2013, MNRAS, 434, 1332

Marshall N., Warwick R. S., Pounds K. A., 1981, MNRAS, 194, 987
Miller L., Turner T. J., Reeves J. N., 2008, A&A, 483, 437
Mitsuda K. et al., 2007, PASJ, 59, 1
Mosquera A. M., Kochanek C. S., Chen B., Dai X., Blackburne J. A., Chartas G., 2013, ApJ, 769, 53
Nardini E., Risaliti G., 2011, MNRAS, 417, 2571
Nardini E., Fabian A. C., Reis R. C., Walton D. J., 2011, MNRAS, 410, 1251
Nardini E. et al., 2015, Science, 347, 860 (N15)
Ohsuga K., Mineshige S., 2011, ApJ, 736, 2
Ohsuga K., Mineshige S., Mori M., Kato Y., 2009, PASJ, 61, L7
Pounds K. A., Reeves J. N., King A. R., Page K. L., O'Brien P. T., Turner M. J. L., 2003, MNRAS, 345, 705
Proga D., Kallman T. R., 2004, ApJ, 616, 688
Proga D., Stone J. M., Kallman T. R., 2000, ApJ, 543, 686
Reeves J. N., O'Brien P. T., Vaughan S., Law-Green D., Ward M., Simpson C., Pounds K. A., Edelson R., 2000, MNRAS, 312, L17
Reeves J. N., O'Brien P. T., Ward M. J., 2003, ApJ, 593, L65
Reeves J. N. et al., 2009, ApJ, 701, 493 (R09)
Reeves J. N. et al., 2014, ApJ, 780, 45 (R14)
Reeves J. N. et al. 2016, ApJ, submitted
Reis R. C., Miller J. M., 2013, ApJ, 769, L7
Risaliti G., Elvis M., Fabbiano G., Baldi A., Zezas A., 2005, ApJ, 623, L93
Risaliti G., Elvis M., Fabbiano G., Baldi A., Zezas A., Salvati M., 2007, ApJ, 659, L111
Risaliti G. et al., 2009, MNRAS, 393, L1
Risaliti G. et al., 2013, Nature, 494, 449
Simpson C., Ward M., O'Brien P., Reeves J., 1999, MNRAS, 303, L23
Takahashi T. et al., 2007, PASJ, 59, 35
Tatum M. M., Turner T. J., Miller L., Reeves J. N., 2013, ApJ, 762, 80
Tombesi F., Cappi M., Reeves J. N., Palumbo G. G. C., Yaqoob T., Braito V., Dadina M., 2010, A&A, 521, A57
Tombesi F., Meléndez M., Veilleux S., Reeves J. N., González-Alfonso E., Reynolds C. S., 2015, Nature, 519, 436
Torres C. A. O., Quast G. R., Coziol R., Jablonski F., de la Reza R., Lépine J. R. D., Gregório-Hetem J., 1997, ApJ, 488, L19
Turner T. J., Reeves J. N., Kraemer S. B., Miller L., 2008, A&A, 483, 161
Turner T. J., Miller L., Kraemer S. B., Reeves J. N., Pounds K. A., 2009, ApJ, 698, 99
Turner T. J., Miller L., Kraemer S. B., Reeves J. N., 2011, ApJ, 733, 48
Vaughan S., Edelson R., Warwick R. S., Uttley P., 2003, MNRAS, 345, 1271
Wilms J., Allen A., McCray R., 2000, ApJ, 542, 914

This paper has been typeset from a TEX/LATEX file prepared by the author.